International Journal of Fatigue 211 (2026) 109747

Contents lists available at ScienceDirect

International Journal of Fatigue

journal homepage: www.elsevier.com/locate/ijfatigue

Corrosion-fatigue of L-PBF Ti-6Al-4V lattice struts: role of geometrical imperfections under simulated physiological conditions[☆]

Farnoosh Farhad [a,1,*], Simone Murchio [b,c,1], Melika Babaei [c], Alessandro Albertini [c], Devid Maniglio [c], Filippo Berto [b], Matteo Benedetti [c,*]

[a] School of Engineering, Physics and Mathematics, Northumbria University, Newcastle upon Tyne, UK
[b] Department of Chemical Engineering Materials Environment – La Sapienza University of Rome, Italy
[c] Department of Industrial Engineering – DII, University of Trento, Trento, Italy

ARTICLE INFO

Keywords:
Additive manufacturing
Ti-6Al-4V
Lattice structures
Corrosion–fatigue
Phosphate-buffered saline
Geometrical imperfections

ABSTRACT

The corrosion-fatigue behaviour of laser powder bed fusion (L-PBF) Ti-6Al-4V lattice struts was investigated with particular emphasis on the role of manufacturing-induced geometrical imperfections. Thin strut specimens representing strut-based lattice sub-unit elements were built at a 60° orientation and tested under tension–tension loading ($R = 0.1$) in laboratory air and in phosphate-buffered saline (PBS) at 37 °C. Micro-computed tomography (Micro-CT) was employed to quantify surface roughness, geometrical deviations, and the interaction between surface valleys and near-surface porosity. Quasi-static tensile tests showed limited scatter in strength and ductility, indicating that monotonic behaviour is governed by global geometry. In contrast, fatigue performance was strongly defect-sensitive. While comparable fatigue strength was observed in air and PBS in the low-cycle regime, exposure to PBS led to a marked reduction in high-cycle fatigue strength, reaching approximately 25% at 10^6 cycles. Fractographic and EDXS analyses revealed that fatigue cracks initiated at surface-connected valleys in both environments, whereas the physiological environment primarily accelerated crack propagation through corrosion-assisted mechanisms and suppressed crack branching. A micro-CT-based deepest-valley analysis showed good agreement between predicted critical defects and experimental failure locations. The results highlight the dominant role of extreme surface geometrical imperfections and environment-assisted crack growth in the fatigue behaviour of L-PBF Ti-6Al-4V lattice structures.

1. Introduction

Porous metallic lattice structures have attracted significant interest for orthopaedic implant applications because they allow mechanical properties to be tailored through geometry rather than material composition alone. In particular, additively manufactured Ti6Al4V lattice structures can achieve substantial reductions in elastic modulus, mitigate stress shielding, and promote bone in-growth through controlled porosity and permeability, while retaining the favourable biocompatibility of titanium alloys [1–12]. Recent studies have further demonstrated the potential of additively manufactured Ti6Al4V lattice structures in orthopaedic applications, including load-bearing implants and bone scaffolds, where controlled porosity enhances osseointegration and long-term biological performance [13–16]. In parallel, increasing attention has been devoted to the characterisation of Ti6Al4V lattice structures, particularly in terms of fatigue behaviour, and defect-driven mechanisms [17,18] However, despite these advantages, the long-term reliability of lattice-based implants remains dominated by their resistance to cyclic loading under physiological conditions, where fatigue rather than static strength controls failure [2,4,5].

The fatigue behaviour of lattice structures differs fundamentally from that of bulk components. Replacing solid geometry with networks of slender struts and nodal junctions reduces the effective load-bearing area and introduces highly localised stress concentrations, particularly at surfaces and geometric discontinuities. As a result, fatigue damage in lattice structures is a strongly localised phenomenon, with crack initiation typically occurring at specific struts or nodal regions rather than

---

[☆] This article is part of a special issue entitled: ‘FDMD 5’ published in International Journal of Fatigue.

[*] Corresponding authors.

E-mail addresses: farnoosh.farhad@northumbria.ac.uk (F. Farhad), matteo.benedetti@unitn.it (M. Benedetti).

[1] Authors contributed equally to this paper as co-first authors.

https://doi.org/10.1016/j.ijfatigue.2026.109747
Received 23 December 2025; Received in revised form 1 April 2026; Accepted 7 May 2026

being governed by global material properties [2,4,5,10,19,20]. This localisation makes systematic fatigue characterisation of full lattice assemblies challenging, both experimentally and analytically, and is made more challenging by the lack of standardised fatigue testing procedures for additively manufactured (AM) cellular materials [2,4,10,11,21].

Among AM technologies, laser Powder Bed Fusion (L-PBF) has become the most widely used manufacturing technique for producing Ti6Al4V lattice structures due to its geometric flexibility and industrial maturity [2,3,5,22,23]. Nevertheless, the layer-by-layer nature of the process inevitably introduces manufacturing-related imperfections, including surface roughness, internal porosity, residual stresses and systematic geometrical imperfections [2,3,19,20,24–27]. These defects are particularly pronounced in lattice structures due to their small feature sizes and short melt line in manufacturing process, and their severity depends strongly on build orientation and local thermal changes caused by laser melting [20,25–27]. Even under optimised processing conditions, such imperfections cannot be fully eliminated and therefore represent an inherent characteristic of L-PBF lattice structures [2,22,23,26].

Among these imperfections, surface roughness and geometrical deviations of struts play a dominant role in fatigue performance. In L-PBF Ti6Al4V strut-based lattices, rough as-built surfaces, partially melted powder particles and orientation-dependent cross-sectional distortions act as micro-notches, leading to high local stress concentrations under cyclic loading [19,20,28]. Fatigue cracks have consistently been shown to initiate at these surface features or internal defects [20,27]. The strong sensitivity of fatigue behaviour to as-built geometry highlights the need for quantitative characterisation of geometrical imperfections rather than reliance on nominal CAD dimensions.

Given the localised nature of fatigue damage, increasing attention has been directed towards testing miniaturised specimens that replicate lattice sub-unital elements, such as individual struts, instead of full lattice assemblies [19,20,25,26,28,29]. Thin-strut specimens provide a controlled experimental framework for isolating surface-driven fatigue mechanisms while avoiding the geometric complexity and load redistribution effects that present in complete lattices. This approach allows systematic investigation of manufacturing-induced variability, including surface texture, porosity and geometrical imperfections, under well-defined uniaxial loading conditions [19,20,25–28]. While such specimens do not fully replicate the multiaxial stress states at nodal junctions, they are particularly effective for studying crack initiation behaviour, which dominates fatigue life in the high-cycle regime relevant to orthopaedic implants.

In addition to manufacturing-related imperfections, the service environment plays a critical role in determining fatigue performance. Orthopaedic implants operate in aqueous, ion-rich physiological environments where cyclic mechanical loading interacts with electrochemical processes at the material surface due to cell adhesions and harsh body fluid environment (Fig. 1). Under such conditions, corrosion fatigue can occur, leading to accelerated crack initiation and propagation compared to fatigue in air [30,31]. In Ti6Al4V, cyclic disruption of the protective oxide layer exposes fresh metal to the environment, enabling corrosion-assisted damage even when individual stress cycles remain below thresholds for stress corrosion cracking [30,31]. These effects are naturally time-dependent and become more pronounced at low loading frequencies, which are representative of physiological conditions during activities such as walking [31–33].

The characteristics of lattice structures are expected to worsen corrosion fatigue effects compared to bulk materials. The high surface area-to-volume ratio of cellular architectures increases the fraction of material exposed to the environment. Also, complex geometries may create geometrical regions where fluid becomes trapped or poorly exchanged, creating a local chemical environment that is different from the surrounding bulk fluid and promote corrosion processes [31,34,35]. Manufacturing-induced surface roughness and geometrical imperfections further provide preferential sites for localised corrosion and subsequent fatigue crack nucleation. Despite this, corrosion fatigue of AM lattice structures has received limited attention [36], and most existing studies consider either fatigue behaviour in air or corrosion effects under static or monotonic loading conditions [2,19,20,28,29,34,37–41].

Fracture surface analysis, i.e. fractography, of L-PBF Ti6Al4V lattices and strut specimens have shown that fatigue cracks predominantly initiate at surface defects, including roughness valleys, partially melted particles and geometric discontinuities, with crack paths strongly influenced by build orientation and surface morphology [19,20,28,29,37]. Environmental exposure can further modify fracture surface features, by encouraging corrosion-assisted crack initiation and altering crack propagation behaviour [30–32,42–45]. However, systematic studies combining three-dimensional characterisation of geometrical imperfections, using Micro-CT, with Scanning Electron Microscopy (SEM) fractography under simulated physiological environments remain infrequent.

The present work investigates the tensile and fatigue behaviour of L-PBF Ti6Al4V strut-based lattice sub-unital elements manufactured at a 60° build orientation. Fatigue tests were conducted under tension–tension loading ($R = 0.1$) both in air at room temperature and in phosphate-buffered saline (PBS) at 37 °C using a bespoke environmental test vessel that accounts for fluid flow, temperature control and minimisation of air entrapment. Micro-CT was employed to quantify geometrical imperfections of the as-built struts, and SEM fractography

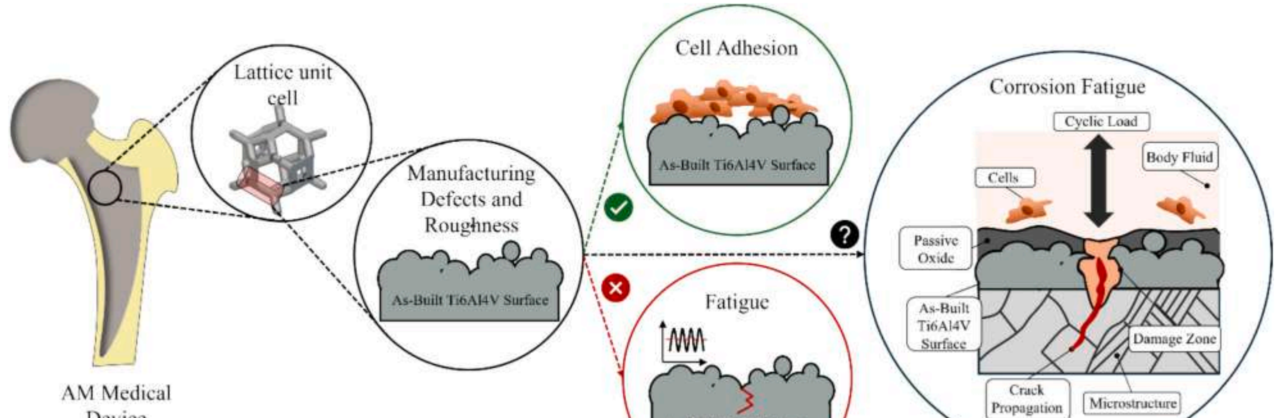

Fig. 1. Corrosion fatigue process at the orthopaedic medical implants.

was used to identify fatigue crack initiation and propagation mechanisms. By correlating geometrical deviations, environmental exposure and fracture behaviour, this study aims to improve understanding of corrosion fatigue failure in additively manufactured Ti6Al4V lattice structures relevant to orthopaedic implant applications.

2. Materials and methods

2.1. Specimen manufacturing and design

Dog-bone specimens mimicking the sub-unit strut of a lattice truss were designed with a nominal diameter of 670 µm and a gauge length of 2.4 mm, as shown in Fig. 2a. The reader is referred to [20,27] for a comprehensive description of the specimen design rationale and its geometric features. Briefly, the specimen consists of a single cylindrical gauge section connected to enlarged gripping regions through filleted transition zones, designed according to the streamline fillet principles described in [46] to minimize stress-concentration effects and prevent premature failure at the grips. The purpose of this specimen geometry is to isolate and investigate the mechanical and corrosion-fatigue behaviour of a single strut, without accounting for the influence of the node/junction region [28,29], which will be addressed in future work.

Biomedical-grade Ti-6Al-4V thin-strut specimens (Grade 5, $O_2 < 0.2\%$, spherical powder 15–45 µm) were manufactured via L-PBF using an EOS M290 system equipped with a 400 W laser, layer thickness of 60 µm, and a printing orientation of 60° with respect to the job plate. The 60° build orientation was intentionally selected as a representative intermediate inclination that well falls within the range of strut inclinations encountered in typical truss-based lattice architectures. This orientation presents an intermediate level of manufacturing-induced geometrical imperfections, arising from stair-stepping and gravitational effects, between the vertically built (90°) and more inclined (45° or 15°) configurations previously characterized in [20]. The printing parameters were industrially optimized to balance productivity and manufacturing quality and are proprietary to our industrial partner, Lincotek Medical S.p.A. The decision to employ these industrially optimized parameters, rather than more accuracy-oriented, research-grade settings, was motivated by the intent to test components representative of real industrial applications. Using thinner layers or highly refined parameter sets would lead to improved geometric accuracy but at the expense of substantially higher build times and reduced industrial relevance.

After manufacturing, a heat treatment above 800 °C was carried out to promote the transformation of the α' martensitic structure into the $\alpha + \beta$ lamellar microstructure. This treatment also served to relieve residual stresses induced during the L-PBF process. The specimens should be regarded as as-built, as no surface finishing treatments were performed. This choice was motivated by two considerations. First, the inherent surface roughness of L-PBF parts is beneficial for orthopaedic applications, as it enhances cell adhesion and proliferation, thereby promoting osteointegration [4]. Second, surface treatments aimed at reducing surface roughness are not always feasible for complex lattice geometries and may not be always compatible with biomedical requirements. It is also worth noting that the as-built surface texture primarily originates from partially melted particles that are metallurgically bonded to the structure, while loosely attached powder particles are

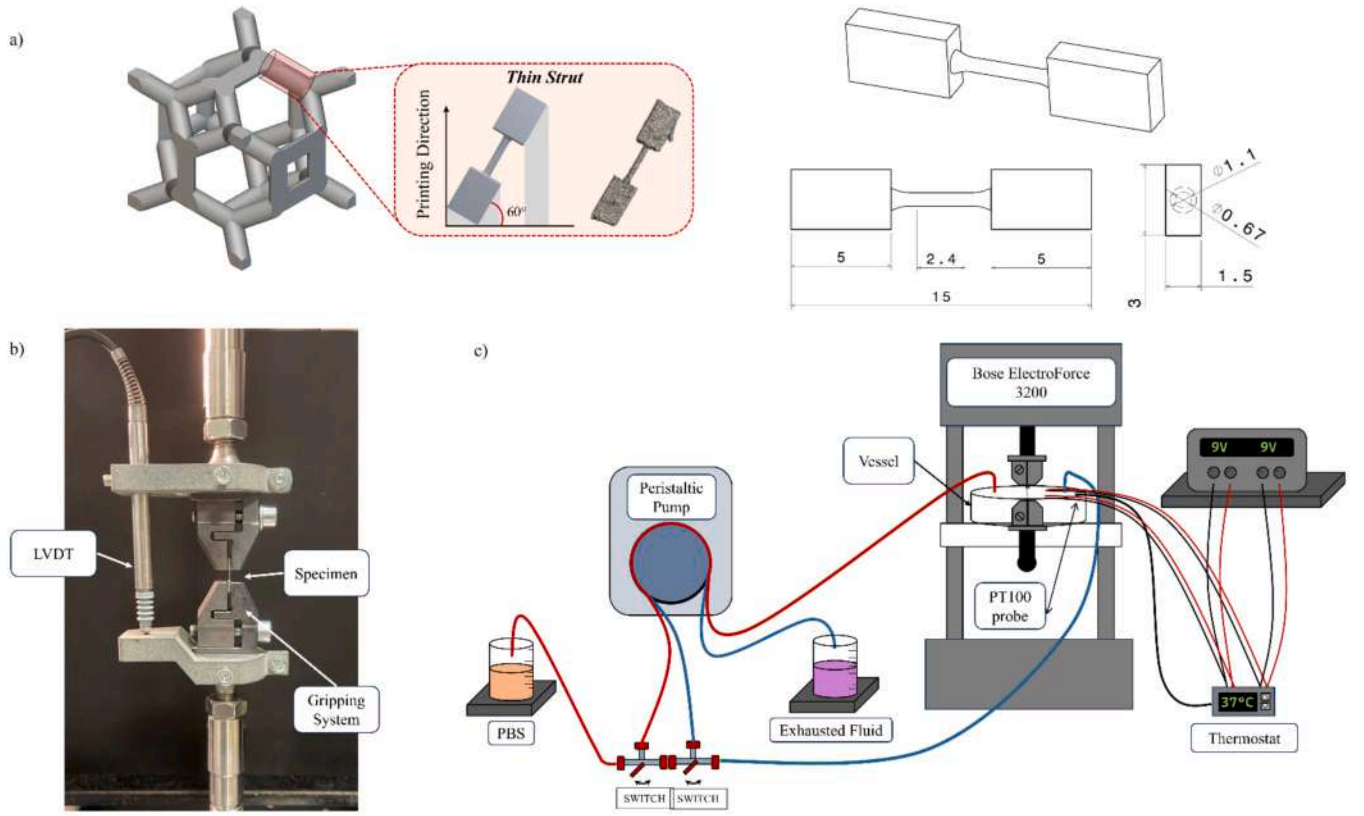

Fig. 2. (a) On the left, schematic of the as-designed specimens built at 60° with respect to the job plate and an optical image of an exemplificative as-built printed specimen., The location of the supporting structures (light grey), placed exclusively on the gripping sections, is highlighted in the as-designed schematic. On the right, 3D isometric view and 2D technical drawing of the thin-strut dog-bone specimens with dimensions reported in mm. The gauge length is 2.4 mm and the nominal diameter is 670 µm. (b) Experimental set-up for quasi-static tensile testing, showing the custom-designed clamping system and the pre-compressed LVDT integrated into the grips for axial deformation measurement. (c) Schematic representation of the corrosion–fatigue testing apparatus, including the PBS reservoir, peristaltic pump, and closed-loop circulation system supplying the testing vessel mounted on the Bose ElectroForce 3200 machine.

typically removed during routine cleaning and sterilization procedures. Supporting structures were placed only at the gripping regions, leaving the gauge length fully unsupported to reproduce the typical printing conditions of lattice components. These supports were then removed using Electrical Discharge Machining (EDM) and wire cutters. Specimens exhibiting unexpected geometrical deviations from the nominal design or interruptions in the gauge length were excluded from the analyses presented in this work.

2.2. *Experimental analysis*

2.2.1. *Morphological characterization*

The stereo-optical approach described in [20,28] was employed for the morphological characterization of the thin-strut specimens. Briefly, the as-built cross-section of each sample was evaluated from two stereo-optical images using an in-house MATLAB (R2024b, The MathWorks, Inc., Natick, MA, USA) image-analysis routine. This procedure enables the extraction of both the "average" cross-sectional area (obtained by averaging all cross-sectional measurements along the gauge length) and the "minimum" cross-sectional area (the smallest value within the gauge region). In addition, the routine quantifies the eccentricity and deviations from the as-designed geometry by assuming that manufacturing-induced effects deform the nominal circular cross-section into an elliptical one. Such deviations arise from gravity-related distortions and stair-stepping effects, which promote parasitic mass accumulation and dross formation on the struts' lowerskin [20,28].

2.2.2. *Micro-CT analyses*

Three-dimensional Micro-computed tomography (micro-CT) scanning was carried out on 4 samples using a Zeiss Xradia Versa 620 system operated at 70 kV and 120 µA, yielding a voxel size of 2.5 µm. The reconstructed volumes were processed using *Dragon*fly 3D World 2025.1 (Comet Technologies Canada Inc., Montreal, QC, Canada; non-commercial license) for surface extraction and porosity analysis.

In method A (Fig. 3a), following reconstruction, segmentation of solid and void phases was performed in *Dragon*fly using Otsu's thresholding method. From both the upper and lower skin surface of each

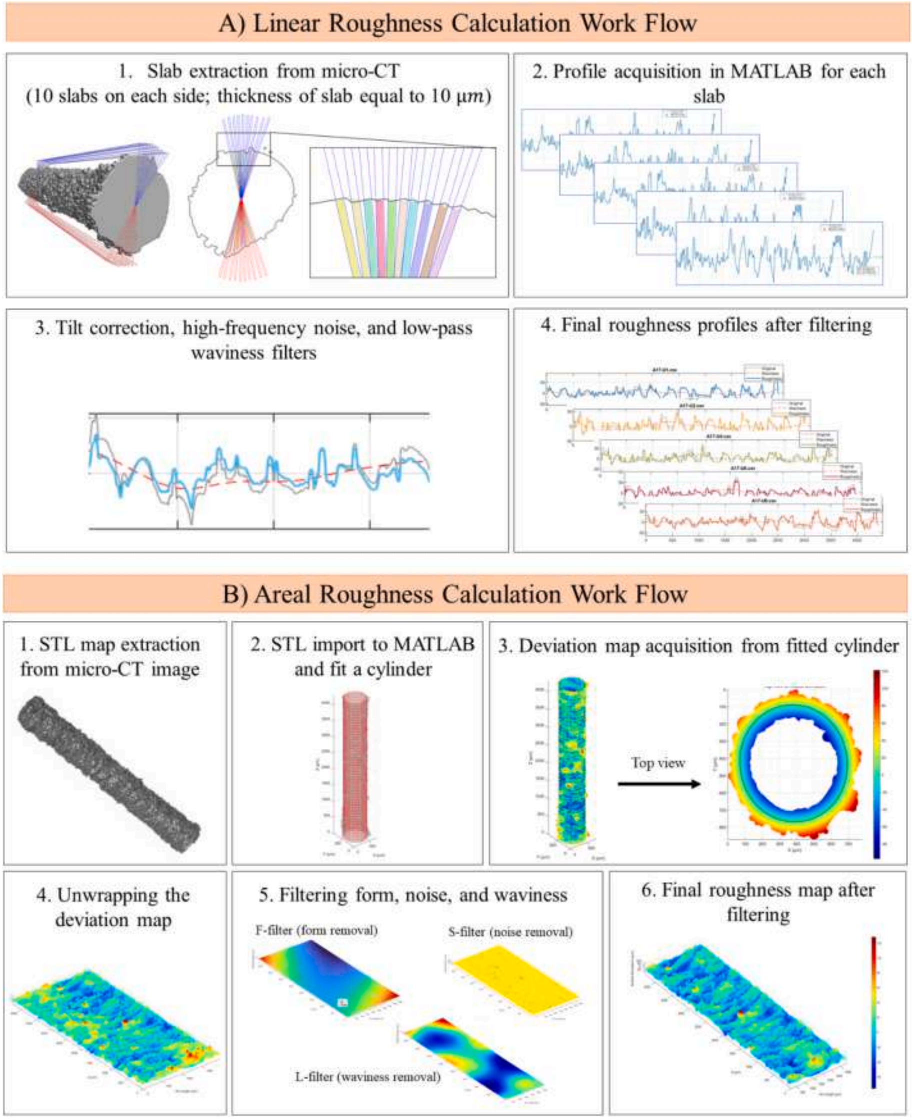

Fig. 3. Workflow for surface roughness analysis using micro-CT data. (a) Linear roughness calculation: (1) extraction of radial slabs from reconstructed micro-CT data; (2) extraction of surface line profiles; (3) application of tilt correction, high-frequency noise filtering, and low-pass waviness filtering; and (4) generation of final filtered roughness profiles. (b) Areal roughness calculation: (1) extraction of the surface mesh from micro-CT; (2) import and elliptical cylinder fitting; (3) computation of radial deviation maps; (4) cylindrical unwrapping into a 2.5D height map; (5) removal of form, noise, and waviness using Gaussian filters; and (6) final areal roughness map representing the spatial distribution of surface deviations.

specimen, 10 regions of interest (ROIs) were defined by extracting slabs with 10 μm thickness (equivalent to four voxels).

Each ROI was analysed using *Dragon*fly's "slice analysis" function to determine the voxel count per micro-CT slice. The resulting data were exported and processed using an in-house MATLAB script (R2024b, The MathWorks, Inc., Natick, MA, USA) to generate and analyse surface profiles. Surface profiles were tilt-corrected and filtered according to ISO 21920 guidelines [47–49]. Gaussian smoothing (smoothdata, Gaussian kernel) was applied to remove high-frequency noise (S-filter) and long-wavelength waviness (L-filter). A short-wavelength cutoff of $\lambda_s = 9$ μm (∼3 × voxel size) was selected following the approach of Thompson et al. [50]. A long-wavelength cutoff of $\lambda_c = 800$ μm was chosen following ASTM F3624–23 [51] which has been shown to sensitively capture surface asperities and adhered particles [50,52]. An evaluation length of 4.4 mm, corresponding to the total measurable length on the sample, was selected. This choice was supported by the findings of Nagalingam et al. [53], which demonstrated that reducing the evaluation length to the minimum cut-off length in AM components does not significantly affect the roughness results (Fig. 3a).

In method B (Fig. 3b), a triangular mesh (.STL) was generated from the micro-CT data using *Dragon*fly's surface determination tool and imported into MATLAB. An elliptical cylinder was fitted to the mesh using nonlinear least squares method, defining the nominal reference geometry. Radial deviations of each mesh vertex from the fitted cylinder were computed and unwrapped into a 2D coordinate frame, producing a height map z(x,y), where x represents circumferential arc length and y the axial coordinate. Following ISO 25178–2 [54], the unwrapped height map was treated as a 2.5D areal surface. Three filtering steps were performed sequentially based on the ASTM F3624–23 [51]: (1) Surface form was removed using polynomial detrending. (2) A Gaussian S-filter ($\lambda_S = 9$ μm) removed high-frequency noise. (3) A Gaussian L-filter ($\lambda_L = 800$ μm) removed long-wavelength waviness.

Subtracting the L-filtered surface from the S-filtered surface yielded the S–L surface containing roughness within the 9–800 μm spatial bandwidth. Areal parameters were computed from the detrended, mean-centred surface according to ISO 25178–2 [54] (Fig. 3b). To further explore this approach, additional methods (Methods C and D) for calculating linear roughness are provided in the Supplementary Materials.

The concept of unwrapping cylindrical structures into a 2.5D surface representation has previously been explored by Oosterbeek et al. [55]. In the present work, we further developed and adapted this approach for our specific samples. All data processing and analysis code used in this study was independently developed by our group.

To identify surface valleys, the "Fill Connected Pores" function was applied to the solid-phase ROI, connecting open surface pores below 100 μm in diameter. This operation connects voxels within a defined distance threshold, effectively linking all open surface pores with diameters below a specified value, depending on the sample's surface imperfections. Subtraction of the "connected pore ROI" and the "solid-phase ROI" was considered as the "valleys ROI".

The Multi-ROI measurement tool was used to rank valleys' depth based on minimum intensity values, reflecting distance from the strut's central axis. Valley depth was computed as the intensity difference between the valley peak and pitch. The deepest 10% of valleys were classified as "critical valleys." Porosity identification followed standard micro-CT practices involving segmentation of void and solid phases [56–59]. Otsu's method was used for thresholding.

Critical valleys were then investigated for possible internal pores in the vicinity. Pores located within a radial distance equivalent to each valley's depth were defined as "critical pores" [60]. Pore-to-valley distances were then calculated. Notably, pores larger than 27 voxels (3 × 3 × 3) were analysed to minimize noise. Critical valleys with or without critical pores in the proximity were investigated as potential fatigue initiation sites (Fig. 4).

Accurately characterizing defect size and morphology remains one of the major challenges in AM components. A commonly adopted approach for quantifying the effective size of an initial defect is the Murakami's parameter, $\sqrt{area}$, which defines the defect area as the projected area of a smooth, equivalent contour perpendicular to the loading direction [61]. However, for defects located near the surface, distinguishing between fully internal defects and those connected to the surface can be challenging, particularly when non-propagating cracks are present and may create an apparent link between a subsurface flaw and the exterior. In this study, the assessment framework provided in BS 7910:2019 [62] was employed to differentiate between single defects and paired

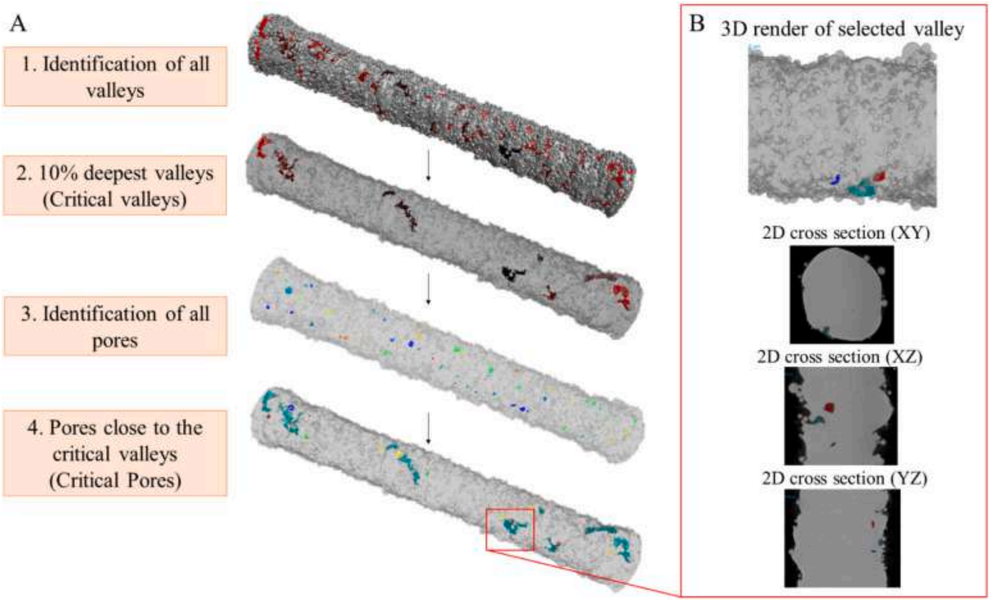

Fig. 4. (a) Workflow for identifying critical surface valleys and associated internal pores using micro-CT analysis. (1) Identification of all surface valleys; (2) selection of the deepest 10% of valleys (critical valleys); (3) segmentation of all internal pores; and (4) identification of pores located within the depth range of the critical valleys (critical pores). (b) A representative critical valley with its associated pores, displayed as a 3D render and orthogonal 2D cross-sections (XY, XZ, and YZ), illustrating pore proximity to the valley and potential crack-initiation geometry.

interacting defects for valleys located in proximity to pores. To simplify the analysis, interactions among neighbouring valleys were not considered, as the valley identification approach inherently treats a cluster of adjacent valleys as a single potential fracture site. Fig. 5 illustrates the relevant section of the BS 7910:2019 standard that defines the criteria for interaction between pores and valleys. Using these criteria, each flaw was classified as either a single defect or an interacting pair for subsequent evaluation. The diameter of each defect was estimated using the "equivalent spherical diameter" function in *Dragonfly*.

As illustrated in Fig. 5 of the standard [62], the effective area of interacting defects is calculated as the surface area of a rectangle that encloses both defects. Although this approach is widely adopted, several recent studies argue that determining the exact projected surface area of defects provides greater accuracy [17,63]. Accordingly, in this work the projected surface area of each defect was computed directly on the plane perpendicular to the stress direction, using "slice analysis" function in XY plane of micro-CT. For interacting pores and valleys, however, the effective area of the distance between the defects, was determined using the criterion specified in [62], consistent with procedures applied in previous studies [62–64].

The effective defect size, $\sqrt{area_{eff}}$, was computed following Murakami et al. [65] and as widely applied in prior literature [63,64,66]. The parameter is defined as:

$$\sqrt{area_{eff}} = \begin{cases} \max\left(\sqrt{area_{R,max}}, \sqrt{area_{D,max}}\right) & if s_1 > a_1 + a_2 \\ \sqrt{area_{R,max}} + \sqrt{area_{D,max}} + s & if s_1 \leq a_1 + a_2 \end{cases} \tag{1}$$

where $\sqrt{area_{D,max}}$ is the maximum projected size of the internal pore, and $\sqrt{area_{R,max}}$ is the maximum projected equivalent size derived from the valley depth [63]. The term s_1 represents the shortest distance between the valley and its adjacent pore, while s represents its vertical component [64]. The terms a_1 and a_2 represent diameter of the pore and diameter of the valley, respectively.

2.2.3. Monotonic Properties: Tensile tests

Quasi-static tensile tests were performed on three specimens using an Instron 5969 universal testing machine (Instron Inc., Norwood, MA, USA) equipped with a 10 kN load cell. Tests were conducted at a constant crosshead speed of 0.5 mm/min, with a data acquisition rate of 2 pts/s. Due to the small dimensions of the miniaturized specimens, a dedicated clamping system was designed and manufactured in-house (see Fig. 2b). The use of a conventional extensometer was not feasible; therefore, axial deformation was monitored using a linear variable differential transformer (LVDT) with a displacement range of 2.5 mm. The LVDT was integrated directly into the custom grips and preloaded prior to each test to ensure measurement repeatability (see Fig. 2b). The Young's modulus was determined from the linear elastic portion of the stress–strain curve, while the yield stress σ_y was obtained using the 0.2% offset method.

2.2.4. Fatigue tests

Two types of fatigue tests were conducted in this study: (i) fatigue tests in air at room temperature and (ii) corrosion–fatigue tests in Phosphate Buffered Saline (PBS) at 37 °C, to simulate physiological conditions [67,68]. PBS was selected since its ionic composition and pH resemble those of human body fluids, as shown in Table 1 in comparison with human blood plasma [68]. Of particular relevance is the comparable concentration of chloride ions (Cl^-), which are known to induce local breakdown of the passive oxide film on titanium alloys, thereby playing a key role in the initiation of corrosion processes under cyclic loading [32]. A 0.01 M PBS solution at pH 7.4 was prepared by dissolving 10 g pouches of PBS powder (P3813, Sigma-Aldrich, USA) in 1 L of distilled (DI) water.

Fatigue and corrosion-fatigue tests were carried out using a Bose Electroforce 3200 testing machine equipped with stainless-steel mechanical grips and a 200 N load cell (sensitivity ± 0.05 N). Both test types were performed under load-controlled tension–tension conditions ($R = 0.1$) using a sinusoidal waveform at a nominal frequency of 1 Hz. The chosen frequency reflects typical physiological loading rates during human gait (1–2 Hz [33]) while ensuring adequate interaction time between the corrosive medium and the specimen.

Corrosion–fatigue tests were performed using the apparatus illustrated in Fig. 2c, consisting of a PBS-filled chamber connected to a circulation system made of PUMPSIL silicone tubing (1.6 mm inner diameter, Watson-Marlow Ltd., UK) and a Rainin Dynamax RP-1 peristaltic pump (Rainin Instruments LLC, USA). This system enables initial chamber filling, drainage of the exhausted solution, and continuous closed-loop circulation throughout testing. The pump was operated at a flow rate of 1.2 mL/min, consistent with values adopted in previous studies [69,70]. The heating system was designed to keep the temperature at 37 ± 1 °C throughout the fatigue test. PBS was pre-heated through a heating plate before the beginning of the test.

Table 1
Chemical composition and pH of human blood plasma [68] and PBS [67].

Composition	Blood Plasma	PBS
Na^+ (mM)	142.0	157
K^+ (mM)	5.0	4.5
Mg^{2+} (mM)	1.5	–
Ca^{2+} (mM)	2.5	–
Cl^- (mM)	103.0	139.7
HCO_3^- (mM)	27.0	–
HPO_4^{2-} (mM)	1.0	11.8
SO_4^{2-} (mM)	0.5	–
pH	7.2–7.4	7.4

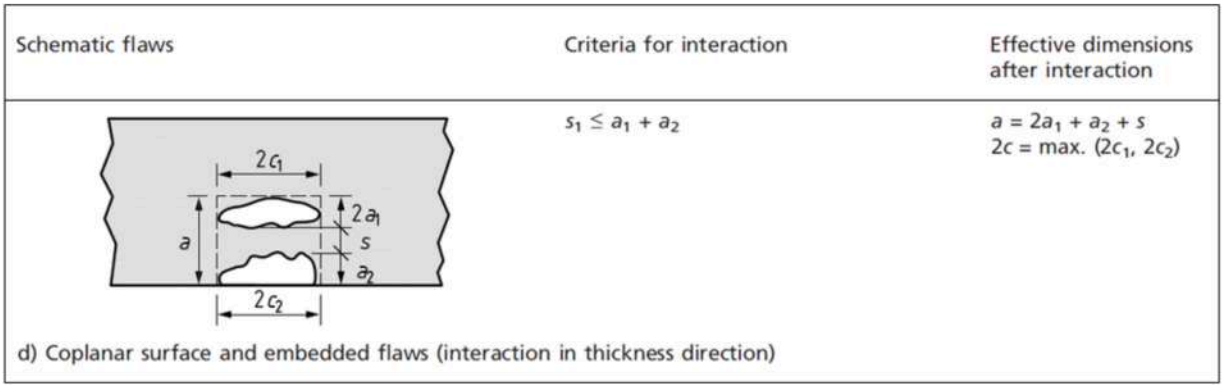

Fig. 5. Defect interaction criteria between surface and internal defects according to BS 7910–2019 standard [62], where s_1 is the minimum distance between defects and s represents its vertical component.

Tests were conducted until specimen failure or until reaching a predefined runout of 10^6 cycles. This runout limit balances the prolonged test durations associated with the low testing frequency with a fatigue life representative of comparative assessment between the two environments. Specimens that survived the runout were indicated with a horizontal arrow on the corresponding S–N curve. It is also worth noting that specimens were not re-tested after runout. Indeed, despite re-testing these specimens could provide additional experimental points and further insight into fatigue resistance mechanisms, they may already contain accumulated damage or corrosion-induced surface modifications, which would influence their subsequent response and limit direct comparison with virgin specimen data. For each Wöhler curve, at least 12 specimens were tested, with 2–3 specimens allocated to each load level. The Wöhler curves were obtained by fitting the experimental data using Eq. (2):

$$\sigma_a = C_1 + \frac{C_2}{N_f^{C_3}} \tag{2}$$

where C_1, C_2, and C_3 are fitting constants, N_f is the number of cycles to failure (or runout), and σ_a is the applied stress amplitude. The 10–90% failure-probability scatter bands were derived according to Eq. (3) using a uniform regression variance over the entire tested range.

$$S^2 = \frac{\sum_{i=1}^{n} \left(\sigma_{a,i} - \widehat{\sigma}_{a,i}\right)^2}{n - p} \tag{3}$$

where $\sigma_{a,i}$ denotes the i-th measured fatigue stress amplitude and $\widehat{\sigma}_{a,i}$ its corresponding regression estimate. The parameters n and p represent, respectively, the total number of experimental data points and the number of fitting coefficients used in Eq. (2), which in this case is three.

2.2.5. *Fracture surface analysis*

A Zeiss Supra 40 (Zeiss, Germany) field-emission scanning electron microscope (FE-SEM) was used to examine the fatigue fracture surfaces of specimens tested both in air and in PBS. Images were acquired in secondary electron mode at an accelerating voltage of 5.00 kV. Prior to analysis, specimens tested in air were ultrasonically cleaned in ethanol for 10 min to remove loose debris, whereas specimens tested in PBS were either cleaned in acetone for 10 min to eliminate residual medium or analysed without any cleaning treatment.

Energy-dispersive X-ray spectroscopy (EDXS) was conducted using a JEOL® JSM-IT300LV SEM (JEOL Ltd., Tokyo, Japan) equipped with a Bruker® QUANTAX EDX system featuring an XFlash® 630 M silicon drift detector (Bruker Nano GmbH, Berlin, Germany). A working distance of 10 mm was employed, and spectra were acquired over an energy range of 0–10 keV using ESPRIT® 2.0 microanalysis software (Bruker Nano GmbH).

3. Results and discussion

3.1. *Morphological characterization*

Fig. 6a presents the bar plot of the cross-sectional measurements obtained from the stereo-optical image analysis described in *Section 2.2.1*. For each specimen, both the minimum cross-section, defined as the smallest cross-section along the gauge length, and the average cross-section, defined as the mean cross-section over the entire gauge length, were computed. These quantities were then averaged over the production batch and compared with the nominal CAD design value. The corresponding percentage deviations from the nominal geometry, together with the cross-sectional eccentricity, are reported in Table 3.

The results indicate that the 60° struts systematically exhibit average cross-sectional areas (0.398 ± 0.035 mm^2) larger than the nominal

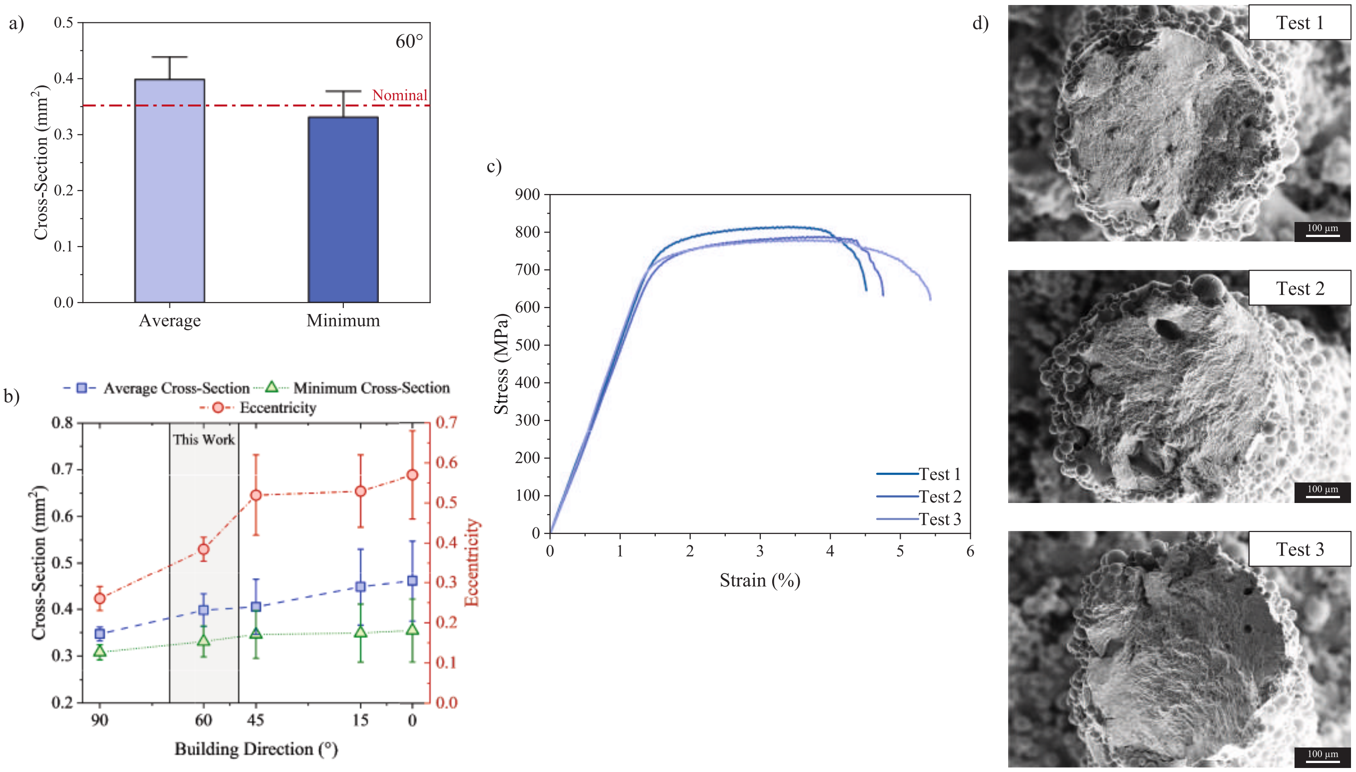

Fig. 6. A) bar plot (mean and standard deviation) of the average and minimum cross-sections measured for the 60° thin strut specimens. the red dashed-dot line indicates the as-design nominal cross-section. (b) comparative plot of the main morphological features (average cross-section, minimum cross section and eccentricity) of thin-strut specimens at 60° (grey area) with respect to thin strut specimens at different building orientations reported in [20]. (c) Stress–strain curves of the quasi-static tensile tests performed on three specimens. (d) SEM fracture surface images of the tested specimens. Scale bars set to 100 µm.

value (0.352 mm^2), whereas the minimum cross-section is slightly undersized (0.331 ± 0.033 mm^2), corresponding to an average deviation of −6 ± 9% with respect to the nominal target. Such behaviour highlights the coexistence of localized geometric thinning within some gauge length regions with an overall increase in material accumulation along the strut length.

Fig. 6b compares the morphological descriptors, namely average and minimum cross-sectional areas and eccentricity, of the 60° thin-strut specimens with those of thin struts manufactured using the same process parameters but oriented at different building angles (90°, 45°, 15°, and 0°), as reported in [20]. The 60° specimens clearly follow the orientation-dependent trends observed for AM struts, exhibiting an intermediate response between the vertically built (90°) and moderately inclined (45°) configurations.

Notably, the 60° struts retain the relatively low eccentricity and higher cross-sectional accuracy typical of the 90° orientation, while simultaneously showing a tendency toward more elliptical cross-sections, characteristic of inclined geometries. Despite this shift toward elliptical shapes, the eccentricity of the 60° specimens remains markedly lower than that of the more steeply inclined and horizontal struts. When considered together with the reduced scatter in cross-sectional measurements and the lower average cross-sectional values compared to the 45° specimens, these results suggest that the lower skin of the 60° struts is less affected by dross formation and parasitic material accumulation. This behaviour can be attributed to a more stable and homogeneous melt pool, in which gravitational and capillary effects are less pronounced than in the 45° orientation. Nevertheless, due to the inclined nature of the 60° specimens, stair-stepping effects are still present, as evidenced by the deviations in cross-sectional size and shape relative to the vertically built (90°) struts.

Table 2 also summarizes the surface roughness values, as mean value and standard deviation on the four CT-scanned specimens. Linear roughness descriptors (Ra, deepest valley Rv, and maximum peak-to-valley Rz) are reported for both the upper and lower strut surfaces of each sample, while areal roughness parameters (Sa, Sv, and Sz) represent the overall surface texture across the entire area. The measured values are consistent with those reported in previous studies on AM lattice structures [27,41,71]. As expected, lowerskin surfaces generally exhibit higher roughness, reflecting the inherently rougher morphology of downward-facing regions generated during the printing process. The influence of surface orientation is more pronounced in Rv and Rz compared with Ra, given that Ra represents an averaged roughness value and is therefore less sensitive to local valleys and peaks [27]. The areal roughness values obtained from the unwrapped Micro-CT-derived surface were slightly higher than the linear roughness values measured along single profiles. This outcome is expected because areal measurements capture height variation in two directions, while a line profile samples only one [72]. As a result, areal analysis includes more surface asperities and provides a more complete representation of topography. This effect is amplified on AM surfaces, which contain multi-directional features, such as partially melted particles, stair-stepping, and melt-pool textures, that may be only partially intersected by a single scan line. Therefore, the higher areal roughness measured here reflects the more comprehensive sampling of surface morphology provided by 2D analysis, rather than processing artifacts.

Table 2
Average and minimum cross-sectional areas, percentage deviation from the nominal CAD design, and eccentricity of 60° thin-strut specimens obtained from stereo-optical image analysis. Data are reported as mean ± standard deviation. Linear (Ra, Rv, Rz) and areal (Sa, Sv, Sz) surface roughness parameters, reported as mean ± standard deviation over four CT-scanned specimens. Linear roughness metrics were evaluated separately for the upper and lower specimen skins.

Cross-Section (mm^2)			**Dev. From CAD (%)**		**Eccentricity (%)**	
Average	**Minimum**		**Average**	**Minimum**	**Average**	**Minimum**
0.398 ± 0.035	0.331 ± 0.033		13 ± 10	−6 ± 9	0.385 ± 0.03	0.282 ± 0.106
Surface Roughness						
Location	**Ra (μm)**	**Rv (μm)**	**Rz (μm)**	**Sa (μm)**	**Sv (μm)**	**Sz (μm)**
Upperskin	12.7 ± 1.3	48.4 ± 6.5	94.0 ± 15.1	15.4 ± 0.5	71.5 ± 4.8	184.9 ± 30.3
Lowerskin	14.3 ± 1.7	41.4 ± 4.2	100.1 ± 11.5			

Table 3
Mechanical properties of 60° thin-strut specimens obtained from quasi-static tensile tests considering the average and the nominal cross-sections: Young's modulus (E), yield stress (σ_y), yield strain (ε_y), ultimate tensile strength (σ_{UTS}), strain at UTS (ε_{UTS}), fracture stress (σ_f), and total elongation to fracture (ε_f). Values are reported as mean ± standard deviation.

Cross Section	**E (GPa)**	**σ_y (MPa)**	**ε_y (%)**	**σ_{UTS} (MPa)**	**ε_{UTS} (%)**	**σ_f (MPa)**	**ε_f (%)**
Average	52 ± 3	733 ± 28	1.6 ± 0.1	794 ± 18	3.6 ± 0.3	632 ± 13	4.9 ± 0.5
Nominal	63 ± 4	880 ± 25	1.9 ± 0.1	954 ± 12	4.4 ± 0.3	760 ± 9	5.9 ± 0.6

3.2. Tensile behaviour

Fig. 6c reports the stress–strain curves of three 60° thin-strut specimens tested under quasi-static tensile loading, while the corresponding mechanical properties (mean values and standard deviations) are summarized in Table 3. Stress values (Fig. 6c) were computed using the average cross-sectional area of each individual specimen, as determined by the stereo-optical approach described in Section 2.2.1. The specimens exhibit an average Young's modulus of 52 ± 3 GPa, which is markedly lower than values typically reported for bulk L-PBF and wrought Ti-6Al-4V, yet consistent with elastic moduli measured for specimens of comparable miniaturized dimensions [20,27,73,74]. Although a consensus regarding the dominant origin of this effect has not yet been reached within the scientific community, it is commonly attributed to one or a combination of factors, including uncertainties in defining the effective load-bearing cross-section [73], the influence of surface roughness and internal defects [75], and size effects associated with the high surface-to-volume ratio intrinsic to miniaturized geometries and their impact on microstructural development.

Yielding occurs at a stress of 733 ± 28 MPa and a corresponding strain of 1.6 ± 0.1%, followed by a limited strain-hardening regime leading to an ultimate tensile strength of 794 ± 18 MPa at 3.6 ± 0.3% strain. Final failure occurs at an average stress of 632 ± 13 MPa and a total elongation to fracture of 4.9 ± 0.5%. For comparison, Table 3 also reports the properties obtained using the nominal cross-section. The nominal area significantly underestimates the actual load-bearing area of the 60° struts, whose measured average cross-section is 0.398 ± 0.035 mm^2 due to manufacturing-induced material accumulation (Table 2), hence resulting in a systematic overestimation of all stress metrics by approximately 16%. The mechanical properties calculated with the average cross-section (Table 3) are in good agreement with those reported for thin L-PBF struts manufactured with the same printing parameters at other inclined orientations [20].

The relatively narrow scatter observed in both strength and strain metrics suggests that, despite the geometric variability typical of L-PBF components (see Fig. 6a-b), the tensile response of the specimens is predominantly ruled by their global structural behaviour rather than by isolated extreme defects. This observation further supports the adoption of the average cross-section as a representative geometric parameter for the interpretation of tensile results, whereas the minimum cross-section, more sensitive to localized geometrical extremes, is employed for the fatigue analysis (Section 3.3), where damage initiation is governed by the most critical cross-section along the gauge length. These data are also corroborated by the SEM fracture surfaces shown in Fig. 6d. All specimens exhibit a cup-and-cone fracture morphology, indicative of a ductile failure mechanism. Gas pores are also observed on the fracture surfaces, suggesting that porosity, combined with cross-sectional shape variations and surface waviness along the gauge length, may act synergistically as the dominant contributors to failure under tensile loading.

3.3. Fatigue behaviour

Fig. 7a presents the S-N curves of L-PBF Ti-6Al-4V thin-strut specimens tested in laboratory air and in PBS solution at 37 °C, considering the minimum cross-sections of each tested specimen. A clear environment-induced degradation in fatigue performance is observed across most of the fatigue life. In the low-cycle fatigue (LCF) regime, fatigue strength remains comparable between the two environments, with only a marginal 3% difference at 2.5×10^4 cycles, where PBS-tested specimens exhibit slightly higher strength. However, in the high-cycle fatigue (HCF) regime, PBS exposure causes pronounced fatigue strength reductions of 18% at 10^5 cycles and 25% at 10^6 cycles relative to air-tested specimens (see Fig. 7b).

This cycle-dependent degradation reflects the interplay between multiple damage mechanisms. While fatigue resistance in air is primarily ruled by as-built surface roughness and L-PBF characteristic internal defects [20,26], PBS testing also introduces additional electrochemical effects. The more consistent fatigue strength reduction observed in the HCF regime can be rationalized by considering that, at the fixed testing frequency of 1 Hz, increasing fatigue life directly corresponds to longer exposure times to the physiological environment. As discussed in greater detail in Section 3.4, crack initiation remains primarily governed by surface-connected geometrical defects in both environments. However, under HCF conditions, where crack propagation constitutes a larger fraction of the total fatigue life, the prolonged exposure allows the PBS environment to interact more extensively with the crack tip, thereby promoting environment-assisted crack propagation through repeated passive film disruption and localized chemical attack. Each cycle of passive film rupture exposes fresh metal to the chloride-rich solution, facilitating localized dissolution and environmentally assisted crack advance. In addition, the longer test duration favors the diffusion of aggressive species into crack tips, further enhancing the electrochemical contribution to crack growth. Conversely, in the LCF regime, the limited number of cycles provides insufficient time for sustained crack-tip/environment interaction, thereby restricting repeated passive film breakdown and preserving fatigue strengths comparable to those measured in air. Based on the data in Fig. 7a, the onset of an appreciable environmental effect can be identified at around 5×10^4 cycles (corresponding to approximately 14 h of testing at 1 Hz), where the fatigue strength reduction is of about 9%. Further electrochemical characterisation (e.g., Electrochemical Impedance Spectroscopy (EIS) or Potentiodynamic Polarisation (PDP)) could provide additional insight into the corrosion behaviour of the structures prior to the application of cyclic loading. Such analyses would help to decouple purely electrochemical effects from corrosion–fatigue mechanisms and will be considered in future work.

Results reported in Fig. 7 are consistent with literature data on corrosion–fatigue behaviour of conventionally manufactured Ti-6Al-4V. Baragetti and Arcieri [43], for instance, reported an approximately 20% reduction in fatigue strength for notched wrought Ti-6Al-4V specimens tested in a 3.5 wt% NaCl solution compared to inert conditions, with the degradation remaining largely independent of the severity of the nominal stress concentration factor (Kt). This observation aligns well with the present findings, indeed, although the tested strut specimens are not notched by design, they inherently exhibit stress concentrations arising from as-built surface irregularities characteristic of the L-PBF process (see Fig. 8), which effectively act as intrinsic micro-notches. Consequently, the Kt-independent environmental degradation reported in [43,45] remains applicable and supports the PBS-induced fatigue strength reduction observed in the present AM components. While the corrosive environments are not identical to [43], PBS contains high concentrations of chloride ions, recognized as the primary agents responsible for corrosion-assisted fatigue damage, thereby further validating this comparison.

The following discussion provides further interpretation of the observed results. When focusing specifically on L-PBF Ti-6Al-4V, it is worth noting that relatively few studies have systematically addressed corrosion fatigue behaviour under physiological environments. Among these, Singh et al. [36] reported a fatigue endurance limit reduction of

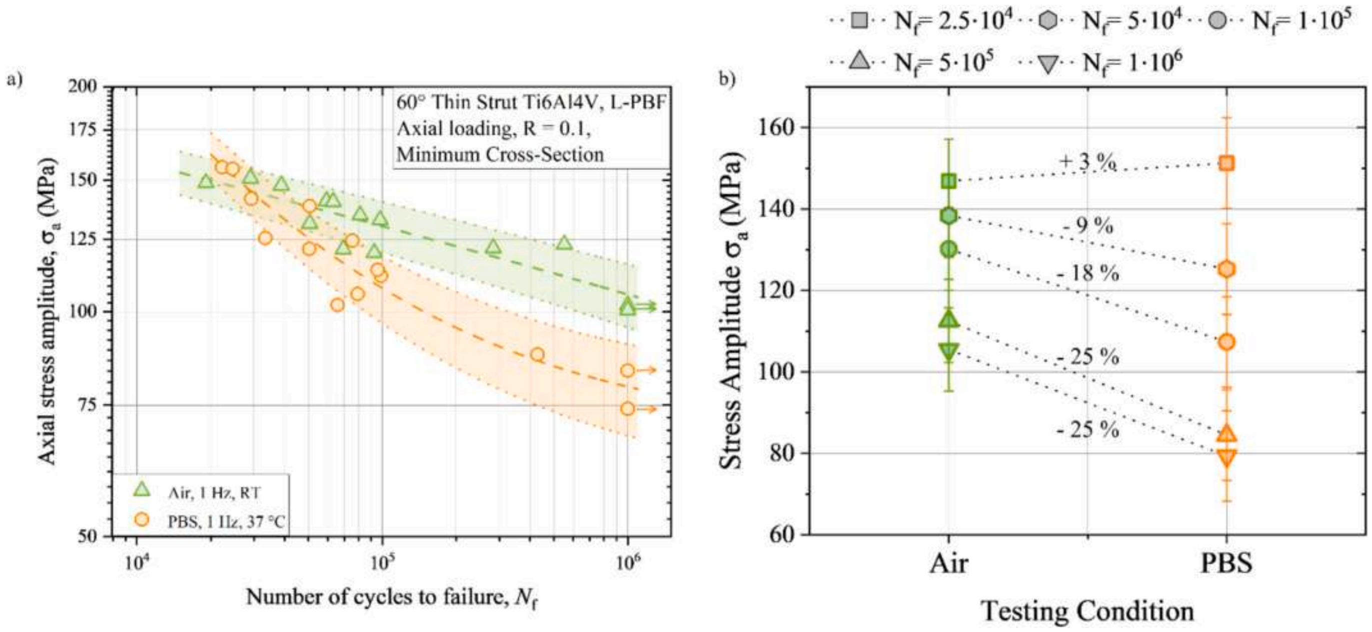

Fig. 7. (a) S–N curves of L-PBF Ti-6Al-4V thin-strut specimens tested in laboratory air and in PBS solution at 37 °C, calculated using the minimum cross-section of each specimen. Run-out specimens at 10^6 cycles are indicated by horizontal arrows. Solid lines represent the fitted Wöhler curves, while shaded bands denote the 10–90% failure probability scatter. (b) Trends derived at 50% failure probability for a fixed number of cycles ($N_f = 2.5 \times 10^4$, 5×10^4, 1×10^5,5×10^5, and 1×10^6). The reported percentage values indicate the relative difference in fatigue strength between specimens tested in PBS and laboratory air.

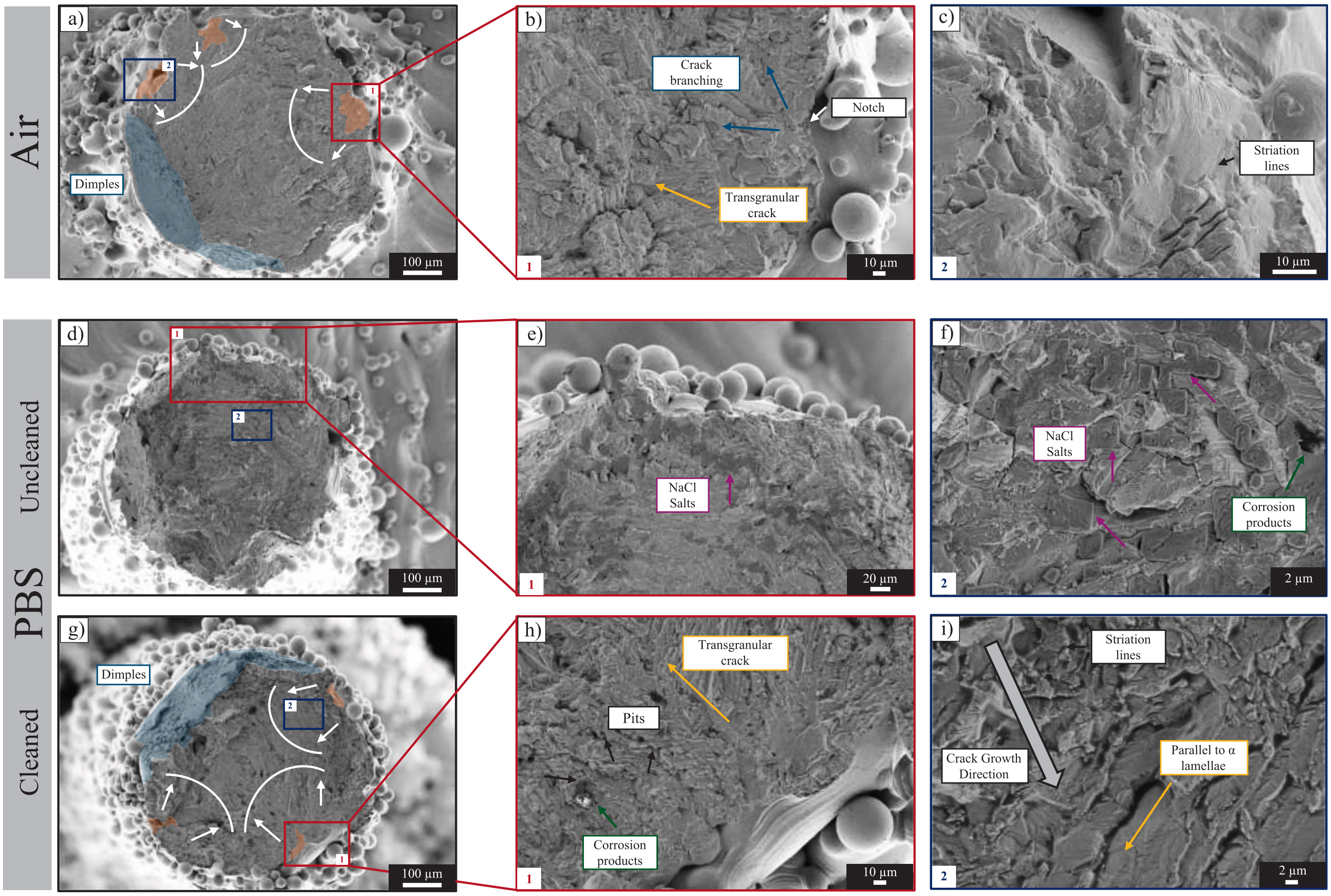

Fig. 8. Representative fracture surfaces of Ti-6Al-4V thin-strut specimens tested in air (a–c) and in PBS at 37 °C (d–i). For PBS, fracture surfaces are shown before (d–f) and after acetone cleaning (g–i). Both specimens failed at about 5 × 10^5 cycles. (a) Air-tested specimen overview showing multiple crack initiation sites at surface-connected defects (orange regions, white arrows) and ductile dimples in the final overload zone (blue region). Scale bar at 100 µm. Red and blue boxes indicate regions shown in (b) and (c), respectively. (b) High-magnification image showing crack branching, transgranular propagation through the α/β lamellar microstructure, and surface-connected notches acting as stress concentrators (image collected from the other fracture half). Scale bar at 10 µm. (c) Fatigue striations near the tip of a lack-of-fusion surface defect. Scale bar at 10 µm. (d) Overview of the uncleaned PBS-tested fracture surface showing NaCl crystallization (dark regions). Scale bar at 100 µm. Red and blue boxes indicate regions shown in (e) and (f). (e–f) High-magnification views of geometrically regular NaCl crystals deposited on the fracture surface. Scale bars at 20 and 2 µm. (g) Overview of the acetone-cleaned PBS-tested fracture surface showing multiple crack initiation sites and ductile dimples. Scale bar at 100 µm. Red and blue boxes indicate regions shown in (h) and (i). (h) Crack propagation region showing transgranular cracking without branching, localized pits, and corrosion products. Scale bar at 10 µm (i) High-magnification view showing fatigue striations and secondary cracks confined to α/β lamellar boundaries perpendicular to the main crack growth direction. Scale bar at 2 µm.

approximately 30% for L-PBF Ti-6Al-4V Neovius lattices tested in simulated body fluid (SBF) compared to air. Notably, this degradation persisted even after surface post-processing by shot peening, highlighting that SBF can markedly compromise fatigue resistance even despite the substantial improvements in surface condition respect to an as-built state. In contrast, Hogg et al. [76] investigated corrosion fatigue behaviour of L-PBF Ti-6Al-4V using rotating-bending tests in Dulbecco's Modified Eagle's Medium (DMEM) and reported a limited influence of the corrosive medium on fatigue performance for as-built specimens. Fatigue failure was shown to be primarily ruled by internal porosity rather than surface-assisted corrosion mechanisms. This apparent discrepancy can be explained by key differences in specimen geometry and testing conditions. The rotating-bending specimens had a nominal gauge diameter of approximately 3.6 mm, for which the relative impact of as-built surface roughness is reduced compared to the sub-millimetric strut specimens investigated in the present work and in lattice-based studies such as [36]. Moreover, the high testing frequency employed by the authors (50 Hz) may have limited the effective interaction time between the corrosive medium and the crack tip, thereby reducing the contribution of corrosion-assisted crack nucleation, which is sensitive to the loading frequency, as reported by *Jesus et al.* [44].

3.4. *Fracture surface analysis*

Fig. 8 presents representative fracture surfaces of specimens tested in air (Fig. 8a-c) and in PBS solution (Fig. 8d-i). For the PBS condition, fracture surfaces are shown both before (Fig. 8d-f) and after acetone cleaning (Fig. 8g-i). The two selected specimens failed at a comparable number of cycles (approximately 5 × 10^5 cycles). Fractographic analysis reveals that fatigue failure initiates from surface-connected defects in both environments, where manufacturing-induced irregularities and as-built surface roughness create stress concentration sites. Multiple crack initiation sites are indeed observed at or near the surface in both conditions, consistent with previous observations on Ti-6Al-4V specimens tested under tension–tension loading at R = 0.1 [20]. Subsurface porosity, as keyhole-type defects, is also present and contributes to crack nucleation and propagation, as evidenced in Fig. 8c, where well-defined fatigue striation marks radiate from the pore edges. Nevertheless, the critical defects responsible for final failure are predominantly surface-connected valleys, as illustrated in Fig. 8b.

Comparison of the crack propagation regions in Fig. 8b (air) and Fig. 8h (PBS) reveals distinct differences in cracking behaviour. In both environments, crack growth proceeds transgranularly through the α/β lamellar microstructure. However, specimens tested in air (Fig. 8b) exhibit crack branching with secondary crack fronts deviating from the main propagation direction. In contrast, this branching phenomenon appears to be suppressed (or limited) in PBS (Fig. 8h), where crack advance follows a more tortuous but direct path. Similar behaviour was reported by *Zhao et al.* [42] for wrought Ti-6Al-4V compact tension specimens tested in simulated body fluid. The authors demonstrated that crack branching and deflection in air increase energy dissipation and effectively reduce fatigue crack growth rates, whereas SBF exposure suppresses secondary crack propagation, resulting in more localized crack advance and consequently in accelerated fatigue crack growth.

The higher-magnification view in Fig. 8i shows the crack propagation region near one of the initiation sites indicated in Fig. 8g (blue box). Secondary cracks are visible along α/β lamellar boundaries oriented perpendicular to the main fatigue crack direction, defined from the clear striation marks. Notably, these secondary cracks remain confined to the fracture surface and do not propagate deeply into the bulk material. This observation is consistent with findings reported in [42], who demonstrated that physiological environments make the α/β lamellar microstructure highly susceptible to corrosion-assisted cracking, with particularly pronounced sensitivity at the α/β phase boundaries. Additionally, the overall fracture surface of specimens tested in PBS (Fig. 8g) appears rougher than those tested in air (Fig. 8a), further highlighting environment-assisted degradation along interphase boundaries during corrosion fatigue. The influence of the corrosive medium is also clearly evident looking at the uncleaned PBS specimen surface (Fig. 8d-f), where darker regions, composed of geometrically regular precipitates, indicate NaCl crystallization on the fracture surface, as shown in Fig. 8f. Moreover, localized pitting and residual corrosion products (likely Al_2O_3 or TiO_2 agglomerates), potentially associated with crevice-induced corrosion [44], are visible on the acetone-cleaned surface (Fig. 8h) near the crack nucleation sites.

To interpret the driving mechanisms ruling the corrosion-fatigue failure behaviour observed in the PBS-tested specimens, detailed EDXS analysis was performed on the fracture surfaces. Fig. 9 reports a comprehensive elemental characterization of a representative specimen that failed at approximately 5×10^4 cycles, lying in the transition region where the environmental effect first becomes appreciable (see Fig. 7b). The back-scattered SEM image in Fig. 9a reveals the fracture morphology of the uncleaned specimen, where two distinct regions (Area 1 and Area 2) can be identified based on their different surface characteristics. The corresponding elemental distribution maps (Fig. 9b-j) provide a qualitative information on the spatial distribution across the whole fracture surface of both the main alloying elements (Ti, Al, and V) and the constituents of the PBS medium (Na, Cl, Ca, K, P, and O).

Titanium (Fig. 9b) and vanadium (Fig. 9d) exhibit relatively homogeneous distributions across the fracture surface, with locally weaker or absent signals in correspondence with internal and surface regions enriched in sodium and chlorine. These regions show a pronounced co-localization of Na and Cl within the same spatial domains, preferentially aligned with features corresponding to crack propagation fronts, and are therefore consistent with the formation of NaCl salt crystals. This interpretation is further confirmed by the EDXS spectrum (Fig. 9m and Table 4) acquired from "Area 2", in Fig. 9k, which reveals elevated Na

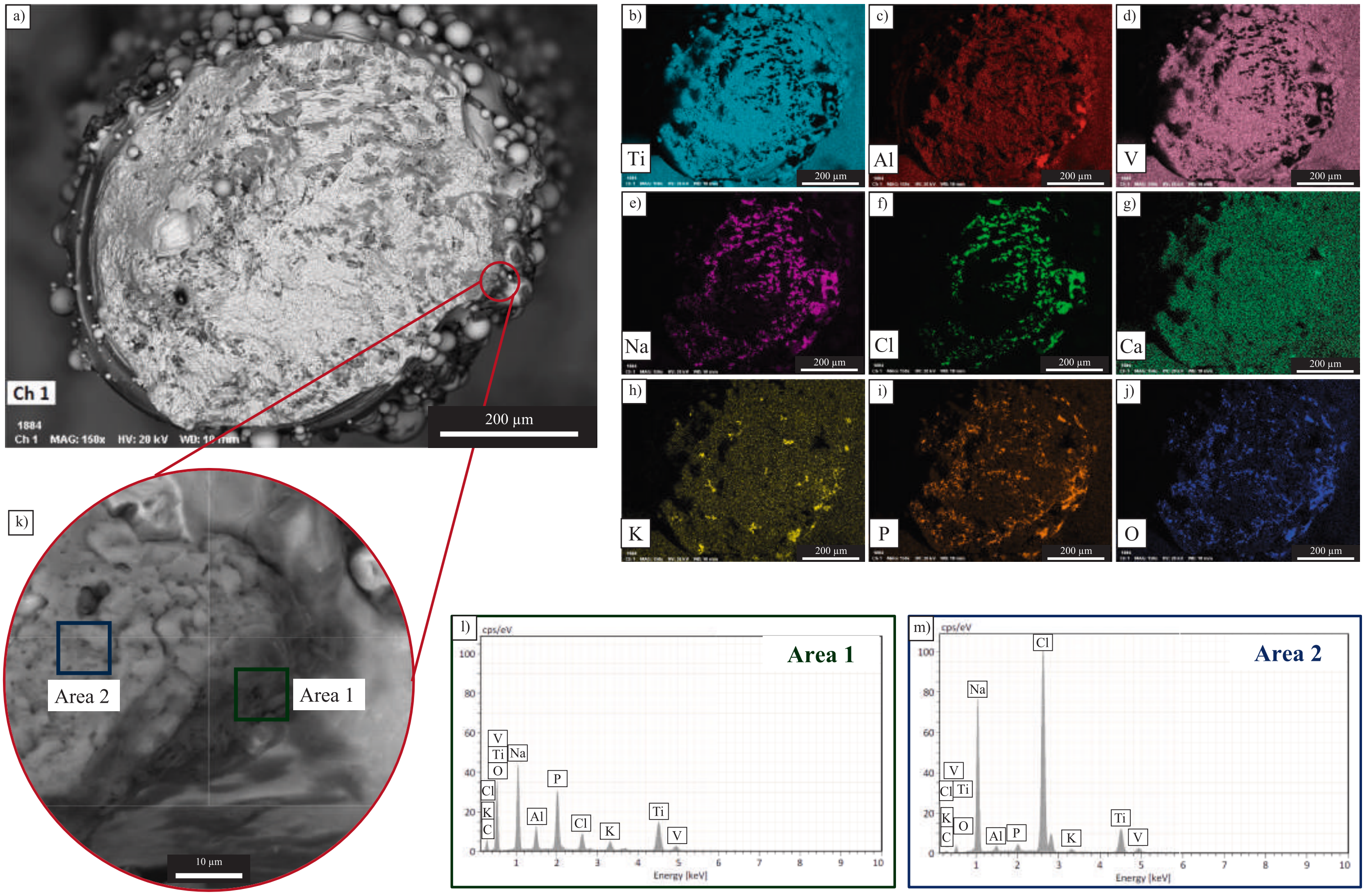

Fig. 9. EDXS elemental characterization of a representative PBS-tested specimen that failed at approximately 5×10^4 cycles. (a) Back-scattered SEM image showing the overall fracture morphology of the uncleaned specimen. Scale bar is set at 200 µm. The red circle indicates the region shown in (k). (b–j) Elemental distribution maps showing the spatial distribution of Ti (b), Al (c), V (d), Na (e), Cl (f), Ca (g), K (h), P (i), and O (j) across the entire fracture surface. Scale bar is set at 200 µm. (k) High-magnification view of the fracture surface showing two distinct regions analysed by EDXS (Area 1 and Area 2) near the crack nucleation site. Scale bar set at 10 µm. (l) EDXS spectrum acquired from Area 1. (m) EDXS spectrum acquired from Area 2.

Table 4
Elemental composition (wt%) from EDXS analysis for Area 1 and Area 2.

wt(%)	C	O	Na	Al	P	Cl	K	Ti	V
Area 1	0.00	44.88	16.72	3.37	9.86	3.92	2.61	17.73	0.27
Area 2	0.00	8.41	27.71	0.86	1.03	46.17	0.97	14.29	0.55

and Cl contents of 27.71 wt% and 46.17 wt%, respectively. The localized nature of this Na–Cl enrichment is particularly significant. If salt deposition were solely the result of post-test drying of the PBS solution, a more uniform distribution of residues would be expected across the exposed fracture surface. Instead, the preferential concentration of chloride-containing species along specific fracture features suggests that Cl^- ions were actively involved during cyclic loading rather than acting merely as passive post-failure residues. Chloride ions are well known to promote the local destabilization of the protective TiO_2 passive film on titanium alloys, facilitating localized electrochemical activity under cyclic mechanical stresses and contributing to the observed reduction in fatigue performance in physiological environments.

Further insight into the crack initiation mechanisms is provided by the spatial distribution of aluminium. Unlike Ti and V, aluminium (Fig. 9c) does not display a uniform distribution but shows localized enrichment, most extensively detected near surface notches that are likely associated with crack nucleation sites. In these same regions, increased signals of oxygen (Fig. 9j) and phosphorus (Fig. 9i) are observed, indicating a localized interaction between the alloy and the PBS environment at the early stages of damage development. This is corroborated by the EDXS spectrum (Fig. 9l and Table 4), acquired from “Area 1” depicted in Fig. 9k. The elemental composition of this region shows increased oxygen (44.88 wt%) and phosphorus (9.86 wt%) contents together with a higher aluminium-to-titanium ratio compared with the spectrum obtained from “Area 2” (Fig. 9m). Such compositional differences indicate a localized chemical modification of the surface at the crack nucleation site, likely associated with corrosion-related surface reactions involving aluminium and/or phosphate oxides. While these features do not necessarily imply the formation of stable corrosion oxides, their presence suggests that environmentally induced surface processes might also contributed to crack initiation, particularly at lower cyclic stress amplitudes, as in the case of the exemplificative specimen in Fig. 9. The relatively short exposure time of this specimen allowed the preservation of such localized corrosion features near nucleation sites, which may not be retained at longer fatigue lives due to prolonged contact with the PBS medium and continued cyclic loading.

Additional factors influencing the corrosion-fatigue response of the investigated specimens are the microstructural state and geometrical size inherent to L-PBF Ti-6Al-4V lattice components. In contrast to wrought alloys, which can be tailored to exhibit equiaxed or bimodal α/β microstructures, L-PBF Ti-6Al-4V typically presents a lamellar $\alpha + \beta$ microstructure resulting from martensitic annealing treatments during post-processing. This microstructural condition has been shown to be particularly susceptible to corrosion-assisted damage in chloride-containing physiological environments, due to the high density of α/β interfaces that facilitate environmentally assisted crack propagation [44]. These effects are further amplified in lattice-based components, where the miniaturized strut dimensions not only lead to a markedly increased surface-to-volume ratio, but also to higher local cooling rates during L-PBF processing, resulting in refined α-lath thickness and reduced microstructural length scales, which have been shown to decrease corrosion resistance in physiological environments relative to bulk specimens [77]. In this context, the present results suggest that the physiological environment primarily accelerates fatigue crack propagation rather than fundamentally altering crack nucleation mechanisms, as initiation remains governed by surface-connected defects intrinsic to the as-built condition. These observations highlight the need for future work integrating fatigue crack growth testing and fracture mechanics-based approaches to define safe design criteria for lattice-based AM prosthetic devices operating under physiological conditions.

3.5. Deepest valley failure analysis

Figs. 10 and 11 present the deepest-valley failure analysis for the four specimens characterised by micro-CT. Fig. 10 shows the results for the two specimens fatigue-tested in air (Samples A17 and A19), which failed at approximately 4×10^4 and 5×10^4 cycles, respectively. Fig. 11 shows the corresponding analysis for the two specimens fatigue tested in PBS (Samples A18 and A20), which failed at approximately 1×10^5 and 3×10^4 cycles, respectively. For each specimen, Figs. 10-11 display the 3D reconstructed micro-CT volume, where the 10% critical valleys identified by the proposed workflow are highlighted in black, and the actual killer valley in red. Notably, the method typically identifies fewer than 20 candidate valleys per sample, representing a substantial reduction in potential failure locations and demonstrating the practicality of the approach.

The scatter plots in Figs. 10 and 11 show the relationship between the effective defect size $\sqrt{area_{eff}}$ and the distance between each valley and the most critical pore. For valleys that did not satisfy the proximity requirement of the first interaction criterion, the pore–valley distance was assigned a value greater than the valley depth (“> valley depth”), consistent with our initial assumption for classifying non-interacting defects. This effective defect size parameter is directly related to the local stress intensity factor and was calculated using the equation presented in Section 2.

For the air-tested sample A17 (see Fig. 10a), fatigue failure originated from the valley associated with the second highest $\sqrt{area_{eff}}$ value, indicating a strong correlation between the predicted critical defect parameter and the actual failure location. SEM and micro-CT cross-sectional images of the fracture surface show consistent features across both techniques, including comparable surface morphologies and pore spatial distributions, as clearly visible in all three section planes.

In sample A19 (see Fig. 10b), fatigue failure initiated at the valley ranked fourth in terms of $\sqrt{area_{eff}}$. This observation further supports the predictive capability of the proposed valley-based fracture assessment approach. SEM and micro-CT images confirm consistent defect characteristics at the failure site. Also in this case, the interaction between a surface valley and a sub-surface pore is likely to have promoted fatigue crack initiation, suggesting that pore–valley interaction plays a critical role in defining the effective fatigue-critical defect, providing physically meaningful basis for identifying high-risk crack initiation sites. Nevertheless, it is worth noting that fatigue failure did not originate from the highest-ranked valley. This behaviour can be attributed to the intrinsically statistical nature of fatigue crack initiation, for which a strict maximum-based criterion is not necessarily expected to be universally predictive. Moreover, local microstructural features may further modulate the local fatigue response and interact with geometrical defects, thereby influencing the effective criticality of individual valleys.

For the PBS-tested samples (see Fig. 11), the prediction accuracy varied between the two specimens. In Sample A20 (see Fig. 11b), the fatigue failure initiated from the valley with the second highest $\sqrt{area_{eff}}$, consistent with the behavior observed in the air-tested samples. In contrast, Sample A18 (see Fig. 11a) did not fail at one of the valleys with the highest $\sqrt{area_{eff}}$ values. Micro-CT analysis revealed that the fracture-initiating “killer” valley does not belong to the 10% deepest valleys but instead falls within approximately the deepest 40% of the valley population. Consequently, the identification of the killer valley using the

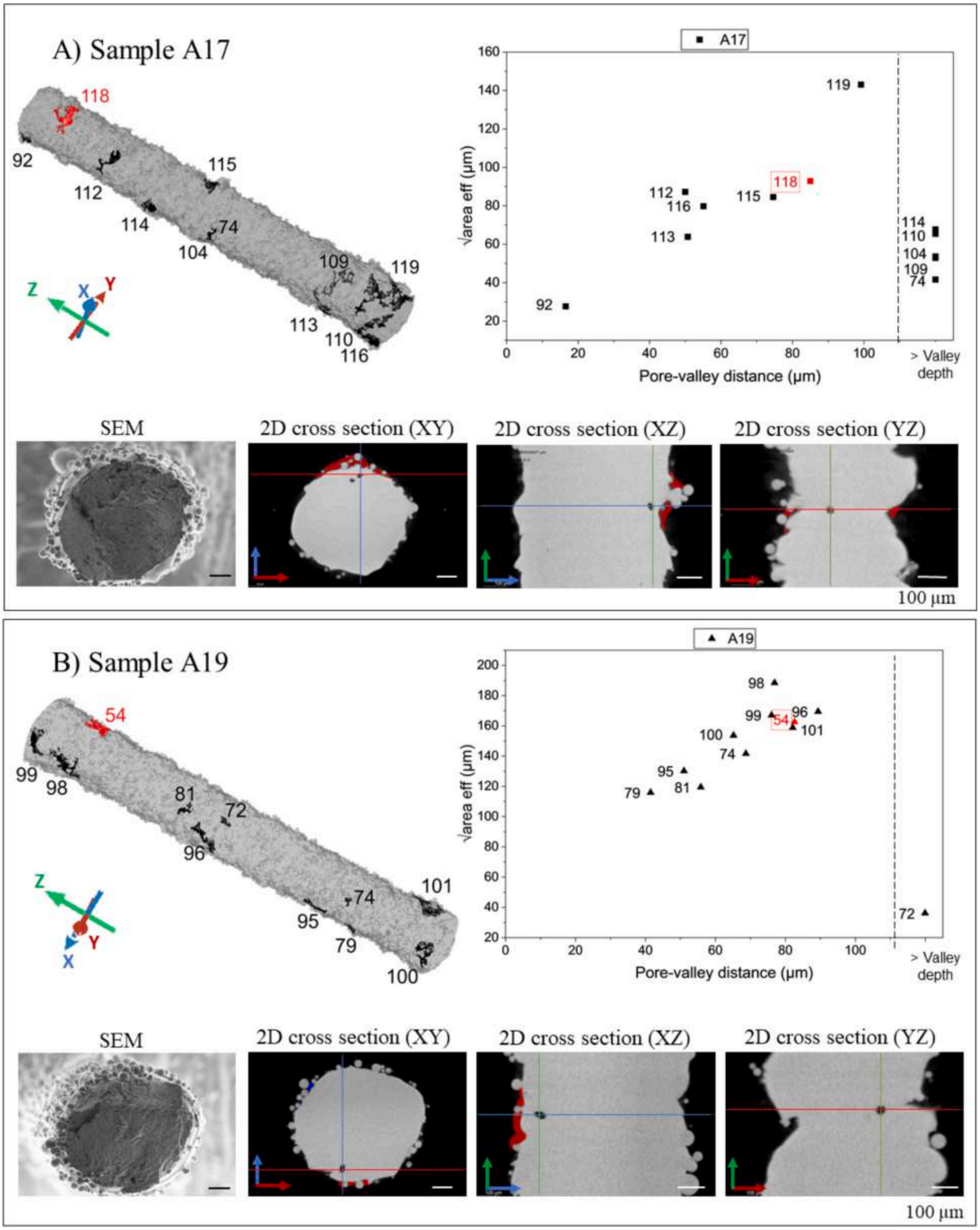

Fig. 10. Valley-based failure analysis for samples tested in air. (a) Sample A17 and (b) Sample A19. For each specimen, the 3D micro-CT reconstruction with detected critical valleys highlighted in black. The killer valley is highlighted in red. The scatter plot shows the $\sqrt{area_{eff}}$ of valley associated with the distance from adjacent pore. The bottom panel provides SEM and micro-CT cross-sectional images of the fracture. The predicted crack-initiating valley is marked in red.

proposed depth-based method was not successful for this specimen. The differing behaviour observed between Samples A18 and A20 can, however, be rationalized in terms of their respective fatigue regimes. Sample A18 failed at approximately 1×10^5 cycles, a fatigue life range in which specimens tested in PBS already exhibit an 18% reduction in fatigue strength (see Fig. 7b). Conversely, Sample A20 experienced predominantly low-cycle fatigue conditions, for which the exposure time is insufficient for the physiological environment to exert a pronounced effect. As a result, the influence of PBS on Sample A20 is expected to be limited or negligible compared to Sample A18, which may

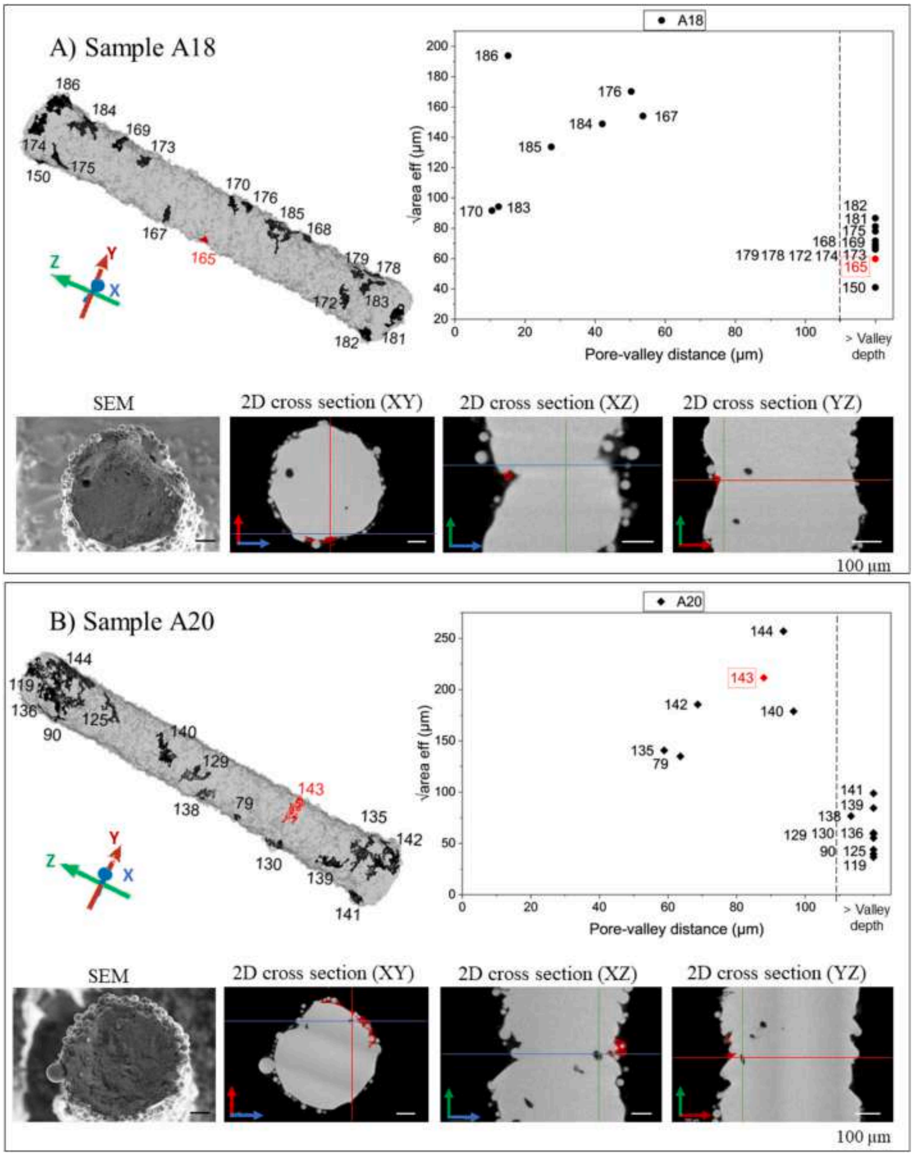

Fig. 11. Valley-based failure analysis for samples tested in PBS. (a) Sample A18 and (b) Sample A20. For each specimen, the 3D micro-CT reconstruction with detected critical valleys highlighted in black. The killer valley is highlighted in red. The scatter plot shows the $\sqrt{area_{eff}}$ of valley associated with the distance from adjacent pore. The bottom panel provides SEM and micro-CT cross-sectional images of the fracture. The predicted crack-initiating valley is marked in red.

explain why Sample A20 exhibits fracture behaviour more closely resembling that of Samples A17 and A19.

Under environmental testing conditions, a surface valley that is not classified as critical based solely on depth may nevertheless become critical. In the case of Sample A18, the fact that the fracture-initiating valley lies within approximately the 40% deepest range, rather than among the deepest 10%, can be rationalized by considering two complementary aspects. First, the current framework relies solely on a valley-depth ranking, not accounting for the valley's local notch root radius. Moderately deep valleys with sharper notch geometries can exhibit higher local stress concentrations than deeper but blunter ones, and may thus govern crack initiation despite a lower depth ranking.

Furthermore, we attribute part of this deviation to limitations inherent to the liquid-chamber setup, which likely restricted PBS flow near the extremities of the strut. As a result, although some valleys near the grips were among the 10% deepest, their limited exposure to the corrosive environment may have reduced their criticality in favour of mid-span valleys with lower depth but subjected to sustained fluid flow. As a matter of fact, it cannot be fully neglected that a prolonged exposure to the corrosive medium, as in the case of specimen A18, may enhance susceptibility to corrosion-assisted degradation at the valley notch root. Such progressive notch sharpening could further increase the effective criticality of valleys not originally considered critical. Moreover, fatigue failure is governed not only by defect severity but also by the local intrinsic material resistance, which is stochastic by nature [78]. In light of these observations, future work will focus on extending the proposed framework by incorporating local stress concentration analysis and reliability-based approaches [78], leveraging CT data acquired both before and after environmental exposure to better characterize the role of the corrosive medium on the evolution of the critical valley notch root radius.

Quantitative assessment of pore size distribution and porosity fraction using micro-CT is now well established, typically relying on segmentation and thresholding of the solid and void phases [56–59]. While pore morphology and total porosity are well studied, the relative spatial positioning of pores within a structure and its influence on mechanical performance remains less understood. Pascual et al. [79] quantified porosity features such as volume, shape, spacing ("gap"), and minimum edge distance (distance between a pore boundary and the specimen surface), and integrated these parameters into finite-element models to predict tensile behaviour. Although minimum edge distance was included, the study did not investigate how pore proximity to surface valleys affects local stress states, which ultimately limited the fracture-site prediction accuracy to 37.5%. Wits et al. [80] likewise identified defect size, shape, and location as primary factors influencing fatigue life, differentiating between surface and subsurface defects but without quantifying precise pore-to-surface distances.

Current literature primarily addresses surface and internal defects independently, leaving a limited understanding of how deep surface valleys (open pores) interact with adjacent internal pores and how their proximity or merging influences crack initiation. Overall, the proposed method in this study demonstrates strong predictive capability, particularly for air-tested specimens. Nevertheless, several opportunities for improvement remain. Increasing the precision of valley identification, refining segmentation protocols, and improving micro-CT resolution, particularly for larger specimens, would likely enhance robustness and reduce uncertainty in the predictions. It is important to emphasize that this method was developed specifically for as-built surfaces, where defects are abundant and valleys are expected to be the most likely fracture-initiating sites. Future work should therefore explore how the approach performs on polished or post-processed surfaces, where the defect landscape differs significantly. One major limitation is the valley-identification process. Because no automated tool currently exists for this purpose, substantial manual intervention was required during segmentation. This procedure is not only time-consuming but also susceptible to reduced precision and lower repeatability. Additionally, the method occasionally identified clusters of valleys rather than isolating a single critical valley, indicating another area where refinement is needed. Finally, there is currently no consensus in the literature regarding the appropriate calculation of the Murakami parameter for interacting defects. Although the present study followed the guidance of the BS 7910 standard, further research is needed to establish a more rigorous and universally accepted approach for such cases.

4. Conclusions

This work examined the corrosion-fatigue behaviour of L-PBF Ti-6Al-4V lattice sub-unit struts manufactured at a 60° build orientation, with specific focus on the role of geometrical imperfections. A combined experimental approach involving micro-CT-based defect characterisation, monotonic tensile testing, fatigue testing in air and in phosphate-buffered saline (PBS) at 37 °C, and detailed fractographic and chemical analyses was adopted.

Morphological analyses revealed systematic geometrical deviations from the nominal design, characterised by pronounced surface roughness, deep surface valleys, and localised minimum cross-sections. While the average cross-section exceeded the nominal value, fatigue performance was governed by extreme geometrical features rather than by mean geometry. Surface-connected valleys, sometimes interacting with near-surface pores, were identified as the dominant fatigue crack initiation sites.

Fatigue tests showed a clear environment-dependent response. While fatigue strength in PBS was comparable to that in air in the low-cycle regime, a pronounced reduction was observed in the high-cycle regime, with a decrease of approximately 25% at 10^6 cycles. This cycle-dependent degradation indicates that environmental effects become increasingly relevant as exposure time increases, consistent with corrosion–fatigue mechanisms.

Fractographic analyses confirmed that crack initiation mechanisms were similar in both environments and controlled by as-built surface defects intrinsic to the L-PBF process. In contrast, the physiological environment significantly influenced crack propagation behaviour. Specimens tested in PBS exhibited reduced crack branching, more localised crack advance, and evidence of corrosion products and chloride-rich deposits along crack paths. EDXS analyses indicated active involvement of chloride ions and local chemical modification near crack initiation and propagation regions, consistent with repeated breakdown of the passive oxide film under cyclic loading.

A deepest-valley failure analysis based on micro-CT data demonstrated good agreement between predicted critical defect severity and experimentally observed failure locations, both in air and in PBS. This finding supports the use of Micro-CT-derived geometrical metrics as a physically meaningful basis for defect-tolerant fatigue assessment of additively manufactured lattice components.

Overall, the results show that the corrosion-fatigue behaviour of L-PBF Ti-6Al-4V lattice struts is controlled by surface-driven crack initiation at geometrical extremes and by environment-assisted crack propagation in physiological media. These findings highlight the necessity of accounting for both manufacturing-induced geometrical imperfections and service environment effects in fatigue design and life prediction of additively manufactured lattice structures. Future work will focus on several directions. First, fatigue crack growth tests on miniaturized strut specimens under both air and PBS conditions should be conducted to quantitatively decouple crack initiation and propagation contributions and to establish environment-specific crack growth rate relationships. Second, the deepest-valley failure prediction methodology can be refined by incorporating automated local stress concentration analysis, progressing from depth-based ranking toward stress-intensity-based criticality assessment. Third, the investigation should be extended to additional build orientations to determine whether the orientation-dependent trends observed in air, where, for $R = 0.1$ loading, fatigue strength decreases monotonically with decreasing build angle, are preserved, amplified, or altered under corrosion–fatigue conditions. Finally, extending the experimental campaign to full lattice components, including nodal junctions, would provide further insight into how the corrosion–fatigue mechanisms identified at the single-strut level can be translated to the structural response of complete lattice architectures.

CRediT authorship contribution statement

Farnoosh Farhad: Writing – review & editing, Writing – original draft, Resources, Methodology, Investigation, Funding acquisition, Formal analysis, Data curation, Conceptualization. **Simone Murchio:** Writing – review & editing, Writing – original draft, Resources, Methodology, Investigation, Formal analysis, Data curation, Conceptualization. **Melika Babaei:** Writing – review & editing, Writing – original draft, Methodology, Formal analysis, Data curation. **Alessandro Albertini:** Investigation, Formal analysis. **Devid Maniglio:** Writing – review & editing, Resources. **Filippo Berto:** Writing – review & editing, Funding acquisition. **Matteo Benedetti:** Writing – review & editing, Resources, Methodology, Conceptualization.

Declaration of competing interest

The authors declare that they have no known competing financial interests or personal relationships that could have appeared to influence the work reported in this paper.

Acknowledgments

The authors gratefully acknowledge the financial support provided by the UK Royal Society International Exchange Grant (IES\R2\222165). Funded by the European Union (ERC, 101093897 Butterfly). Views and opinions expressed are however those of the author(s) only and do not necessarily reflect those of the European Union or the European Research Council Executive Agency. Neither the European Union nor the granting authority can be held responsible for them. The authors also acknowledge.

Sheffield Tomography Centre and University of Sheffield funding from EPSRC (EP/T006390/1) and the technical support and facilities at

Northumbria University and University of Trento that enabled the experimental work presented in this study. MB and SM would also like to thank Lincotek's Medical S.p.A. for the manufacturing of the specimens.

Appendix A. Supplementary data

Supplementary data to this article can be found online at https://doi.org/10.1016/j.ijfatigue.2026.109747.

Data availability

Data will be made available on request.

References

[1] Surjadi JU, Gao L, Du H, Li X, Xiong X, Fang NX, et al. Mechanical Metamaterials and their Engineering applications. Adv Eng Mater 2019;21. https://doi.org/10.1002/adem.201800864.

[2] Benedetti M, du Plessis A, Ritchie RO, Dallago M, Razavi N, Berto F. Architected cellular materials: a review on their mechanical properties towards fatigue-tolerant design and fabrication. Materials Science and Engineering: R: Reports 2021;144:100606. https://doi.org/10.1016/j.mser.2021.100606.

[3] du Plessis A, Razavi N, Benedetti M, Murchio S, Leary M, Watson M, et al. Properties and applications of additively manufactured metallic cellular materials: a review. Prog Mater Sci 2022;125:100918. https://doi.org/10.1016/j.pmatsci.2021.100918.

[4] Babaei M, Murchio S, Emanuelli L, De Biasi R, Branca Vergano L, Giuliani R, et al. Metal additive manufacturing of lattice-based orthopedic implants: a comprehensive review of requirements and design strategies. Materials Science and Engineering: R: Reports 2025;166:101075. https://doi.org/10.1016/j.mser.2025.101075.

[5] Vyavahare S, Mahesh V, Mahesh V, Harursampath D. Additively manufactured meta-biomaterials: a state-of-the-art review. Compos Struct 2023;305:116491. https://doi.org/10.1016/j.compstruct.2022.116491.

[6] Tan XP, Tan YJ, Chow CSL, Tor SB, Yeong WY. Metallic powder-bed based 3D printing of cellular scaffolds for orthopaedic implants: a state-of-the-art review on manufacturing, topological design, mechanical properties and biocompatibility. Mater Sci Eng C 2017;76:1328–43. https://doi.org/10.1016/j.msec.2017.02.094.

[7] Marin E, Lanzutti A. Biomedical applications of Titanium Alloys: a Comprehensive Review. Materials 2023;17:114. https://doi.org/10.3390/ma17010114.

[8] Barba D, Alabort E, Reed RC. Synthetic bone: Design by additive manufacturing. Acta Biomater 2019;97:637–56. https://doi.org/10.1016/j.actbio.2019.07.049.

[9] Cortis G, Mileti I, Nalli F, Palermo E, Cortese L. Additive manufacturing structural redesign of hip prostheses for stress-shielding reduction and improved functionality and safety. Mech Mater 2022;165:104173. https://doi.org/10.1016/j.mechmat.2021.104173.

[10] Amin Yavari S, Wauthle R, van der Stok J, Riemslag AC, Janssen M, Mulier M, et al. Fatigue behavior of porous biomaterials manufactured using selective laser melting. Mater Sci Eng C 2013;33:4849–58. https://doi.org/10.1016/j.msec.2013.08.006.

[11] Zadpoor AA. Mechanical performance of additively manufactured meta-biomaterials. Acta Biomater 2019;85:41–59. https://doi.org/10.1016/j.actbio.2018.12.038.

[12] Cutolo A, Van Hooreweder B. Fatigue behaviour of diamond based Ti-6Al-4V lattice structures produced by laser powder bed fusion: on the effect of load direction. Mater Today Commun 2022;33:104661. https://doi.org/10.1016/j.mtcomm.2022.104661.

[13] Zhang L, Hu H, Wang Q, Zhou J, Liu Y, Li Z, et al. Additively manufactured porous Ti6Al4V Alloy with excellent mechanical properties, corrosion resistance, in vitro and in vivo biocompatibility. J Alloy Compd 2024:1009. https://doi.org/10.1016/j.jallcom.2024.176982.

[14] Koju N, Niraula S, Fotovvati B. Additively Manufactured Porous Ti6Al4V for Bone Implants: a Review. Metals (Basel) 2022;12. https://doi.org/10.3390/met12040687.

[15] Taniguchi N, Fujibayashi S, Takemoto M, Sasaki K, Otsuki B, Nakamura T, et al. Effect of pore size on bone ingrowth into porous titanium implants fabricated by additive manufacturing: an in vivo experiment. Mater Sci Eng C 2016;59:690–701. https://doi.org/10.1016/j.msec.2015.10.069.

[16] Toosi S, Javid-Naderi MJ, Tamayol A, Ebrahimzadeh MH, Yaghoubian S, Mousavi Shaegh SA. Additively manufactured porous scaffolds by design for treatment of bone defects. Front Bioeng Biotechnol 2023;11. https://doi.org/10.3389/fbioe.2023.1252636.

[17] Collini F, Meneghetti G. Towards a fracture mechanics-based fatigue assessment of lattice structures obtained from additive manufacturing of metallic powders. Mater Des 2024;244. https://doi.org/10.1016/j.matdes.2024.113077.

[18] Stammkötter S, Mrzljak S, Koch A, Walther F. Fatigue assessment and damage evolution of additively manufactured Ti–6Al–4V lattice structures for medical applications. J Mater Res Technol 2025;36:3007–14. https://doi.org/10.1016/j.jmrt.2025.03.216.

[19] De Biasi R, Murchio S, Sbettega E, Carmignato S, Luchin V, Benedetti M. Efficient optimization framework for L-PBF fatigue enhanced Ti6Al4V lattice component. Mater Des 2023;230:111975. https://doi.org/10.1016/j.matdes.2023.111975.

[20] Murchio S, Du Plessis A, Luchin A, Maniglio D, Benedetti M. Influence of mean stress and building orientation on the fatigue properties of sub-unital thin-strut miniaturized Ti6Al4V specimens additively manufactured via Laser-Powder Bed Fusion. Int J Fatigue 2024;180. https://doi.org/10.1016/j.ijfatigue.2023.108102.

[21] Gebre NM, De Biasi R, Rita DA, Santus C, Romanelli L, Neri P, et al. Towards standardization of tensile testing for strut-based lattices using compensated beam modeling and strain-energy-based optimization. Mater Des 2025;258:114696. https://doi.org/10.1016/j.matdes.2025.114696.

[22] DebRoy T, Wei HL, Zuback JS, Mukherjee T, Elmer JW, Milewski JO, et al. Additive manufacturing of metallic components – Process, structure and properties. Prog Mater Sci 2018;92:112–224. https://doi.org/10.1016/j.pmatsci.2017.10.001.

[23] Nguyen HD, Pramanik A, Basak AK, Dong Y, Prakash C, Debnath S, et al. A critical review on additive manufacturing of Ti-6Al-4V alloy: microstructure and mechanical properties. J Mater Res Technol 2022;18:4641–61. https://doi.org/10.1016/j.jmrt.2022.04.055.

[24] Shipley H, McDonnell D, Culleton M, Coull R, Lupoi R, O'Donnell G, et al. Optimisation of process parameters to address fundamental challenges during selective laser melting of Ti-6Al-4V: a review. Int J Mach Tool Manuf 2018;128:1–20. https://doi.org/10.1016/j.ijmachtools.2018.01.003.

[25] Pérez-Sánchez A, Yánez A, Cuadrado A, Martel O, Nuño N. Fatigue behaviour and equivalent diameter of single Ti-6Al-4V struts fabricated by Electron Bean Melting orientated to porous lattice structures. Mater Des 2018;155:106–15. https://doi.org/10.1016/j.matdes.2018.05.066.

[26] Aiza I, Baldi C, de la Vega FM, Sebastiani S, Veronese NE, Yousefi M, et al. Effects of build orientation and inclined features on physical, microstructural and mechanical properties of powder bed fusion additively manufactured metallic parts. Prog Mater Sci 2025;147. https://doi.org/10.1016/j.pmatsci.2024.101357.

[27] Murchio S, Dallago M, Zanini F, Carmignato S, Zappini G, Berto F, et al. Additively manufactured Ti–6Al–4V thin struts via laser powder bed fusion: effect of building orientation on geometrical accuracy and mechanical properties. J Mech Behav Biomed Mater 2021;119:104495. https://doi.org/10.1016/j.jmbbm.2021.104495.

[28] Murchio S, Benedetti M, Dallago M, Raghavendra S, Zappini G, Pasini D. Mitigating manufacturing defects in laser-powder bed fusion: a design-led compensation framework for truss-based metallic lattices. J Intell Manuf 2025. https://doi.org/10.1007/s10845-025-02667-5.

[29] Murchio S, Dallago M, Rigatti A, Luchin V, Berto F, Maniglio D, et al. On the effect of the node and building orientation on the fatigue behavior of L-PBF Ti6Al4V lattice structure sub-unital elements. Material Design and Processing Communications 2021;3:1–9. https://doi.org/10.1002/mdp2.258.

[30] Pedeferri P. Corrosion Science and Engineering. Cham: Springer International Publishing; 2018. Doi: 10.1007/978-3-319-97625-9.

[31] McCafferty E. Introduction to Corrosion Science. New York, NY: Springer New York; 2010. Doi: 10.1007/978-1-4419-0455-3.

[32] Dawson DB, Pelloux RM. Corrosion fatigue crack growth of titanium alloys in aqueous environments. Metallurgical Transactions 1974;5:723–31. https://doi.org/10.1007/BF02644669.

[33] Pachi A, Ji T. Frequency and Velocity of people walking. Structural Engineer 2005;83:36–40.

[34] Puttonen T, Chekurov S, Kuva J, Björkstrand R, Partanen J, Salmi M. Influence of feature size and shape on corrosion of 316L lattice structures fabricated by laser powder bed fusion. Addit Manuf 2023;61:103288. https://doi.org/10.1016/j.addma.2022.103288.

[35] Wegner N, Kotzem D, Wessarges Y, Emminghaus N, Hoff C, Tenkamp J, et al. Corrosion and Corrosion Fatigue Properties of Additively Manufactured Magnesium Alloy WE43 in Comparison to Titanium Alloy Ti-6Al-4V in Physiological Environment. Materials 2019;12:2892. https://doi.org/10.3390/ma12182892.

[36] Singh S, Jain J, Yadav SK, Kumar P, Meena VK, Vashisth P, et al. Evaluation of Fatigue Life of Additively Manufactured Ti6Al4V Neovius Lattices in simulated Body Fluid for Biomedical applications. Adv Eng Mater 2025;27. https://doi.org/10.1002/adem.202402368.

[37] Dallago M, Winiarski B, Zanini F, Carmignato S, Benedetti M. On the effect of geometrical imperfections and defects on the fatigue strength of cellular lattice structures additively manufactured via Selective Laser Melting. Int J Fatigue 2019;124:348–60. https://doi.org/10.1016/j.ijfatigue.2019.03.019.

[38] Dallago M, Raghavendra S, Luchin V, Zappini G, Pasini D, Benedetti M. The role of node fillet, unit-cell size and strut orientation on the fatigue strength of Ti-6Al-4V lattice materials additively manufactured via laser powder bed fusion. Int J Fatigue 2021;142:105946. https://doi.org/10.1016/j.ijfatigue.2020.105946.

[39] Chastand V, Tezenas A, Cadoret Y, Quaegebeur P, Maia W, Charkaluk E. Fatigue characterization of Titanium Ti-6Al-4V samples produced by Additive Manufacturing. Procedia Struct Integrity 2016;2:3168–76. https://doi.org/10.1016/j.prostr.2016.06.395.

[40] Nakatani M, Masuo H, Tanaka Y, Murakami Y. Effect of Surface Roughness on Fatigue Strength of Ti-6Al-4V Alloy Manufactured by Additive Manufacturing. Procedia Struct Integrity 2019;19:294–301. https://doi.org/10.1016/j.prostr.2019.12.032.

[41] Pegues J, Roach M, Scott Williamson R, Shamsaei N. Surface roughness effects on the fatigue strength of additively manufactured Ti-6Al-4V. Int J Fatigue 2018;116:543–52. https://doi.org/10.1016/j.ijfatigue.2018.07.013.

[42] Zhao X, Song X, Wang R, Wang L, Liu Y, Hu J. Microstructure-dependent corrosion fatigue crack growth behavior of Ti-6Al-4V alloy in simulated body fluid. Eng Fail Anal 2023;148. https://doi.org/10.1016/j.engfailanal.2023.107184.

[43] Baragetti S, Arcieri EV. Corrosion fatigue behavior of Ti-6Al-4 V: Chemical and mechanical driving forces. Int J Fatigue 2018;112:301–7. https://doi.org/10.1016/j.ijfatigue.2018.02.033.

[44] Jesus JS, Borrego LP, Ferreira JAM, Costa JD, Capela C. Fatigue crack growth under corrosive environments of Ti-6Al-4V specimens produced by SLM. Eng Fail Anal 2020;118. https://doi.org/10.1016/j.engfailanal.2020.104852.

[45] Baragetti S. Notch corrosion fatigue behavior of Ti-6Al-4V. Materials 2014;7:4349–66. https://doi.org/10.3390/ma7064349.

[46] Pilkey WD, Pilkey DF. Peterson's stress Concentration Factors. John Wiley & Sons; 2008.

[47] International Standard Organization. ISO 21920-3:2021 Geometrical product specifications (GPS) — Surface texture: Profile Part 3: Specification operators 2021. https://www.iso.org/standard/72228.html (accessed October 29, 2025).

[48] International Standard Organization. ISO 21920-1:2021 Geometrical product specifications (GPS) — Surface texture: Profile Part 1: Indication of surface texture 2021. https://www.iso.org/standard/72196.html (accessed October 29, 2025).

[49] International Standardization Organization. ISO 21920-2:2021 Geometrical product specifications (GPS) Surface texture: Profile Part 2: Terms, definitions and surface texture parameters 2021.

[50] Thompson A, Newton L, Leach R. New Standard for Metal Powder Bed Fusion Surface Texture Measurement and Characterisation. Metrology 2023;3:237–45. https://doi.org/10.3390/metrology3020013.

[51] ASTM International. ASTM F3624-23 Standard Guide for Additive Manufacturing of Metals – Powder Bed Fusion – Measurement and Characterization of Surface Texture 2023. https://store.astm.org/f3624-23.html (accessed October 29, 2025).

[52] Metelkova J, Vanmunster L, Haitjema H, Van Hooreweder B. Texture of inclined up-facing surfaces in laser powder bed fusion of metals. Addit Manuf 2021;42:101970. https://doi.org/10.1016/j.addma.2021.101970.

[53] Nagalingam AP, Vohra MS, Kapur P, Yeo SH. Effect of Cut-off, Evaluation Length, and Measurement Area in Profile and Areal Surface Texture Characterization of As-built Metal Additive Manufactured Components. Appl Sci 2021;11:5089. https://doi.org/10.3390/app11115089.

[54] International Standard Organization. ISO 25178-2:2021 Geometrical product specifications (GPS) — Surface texture: Areal Part 2: Terms, definitions and surface texture parameters 2021. https://www.iso.org/standard/74591.html (accessed October 29, 2025).

[55] Oosterbeek RN, StrutSurf JJ. A tool for analysis of strut morphology and surface roughness in additively manufactured lattices. SoftwareX 2022;18. https://doi.org/10.1016/j.softx.2022.101043.

[56] du Plessis A, Yadroitsev I, Yadroitsava I, Le Roux SG. X-Ray Microcomputed Tomography in Additive Manufacturing: a Review of the Current Technology and applications. 3D Print Addit Manuf 2018;5:227–47. https://doi.org/10.1089/3dp.2018.0060.

[57] Gobert C, Kudzal A, Sietins J, Mock C, Sun J, McWilliams B. Porosity segmentation in X-ray computed tomography scans of metal additively manufactured specimens with machine learning. Addit Manuf 2020;36:101460. https://doi.org/10.1016/j.addma.2020.101460.

[58] Shange M, Yadroitsava I, du Plessis A, Yadroitsev I. Roughness and Near-Surface Porosity of Unsupported Overhangs Produced by High-speed Laser Powder Bed Fusion. 3D Print Addit Manuf 2022;9:288–300. https://doi.org/10.1089/3dp.2020.0097.

[59] du Plessis A. Effects of process parameters on porosity in laser powder bed fusion revealed by X-ray tomography. Addit Manuf 2019;30:100871. https://doi.org/10.1016/j.addma.2019.100871.

[60] Beretta S. More than 25 years of extreme value statistics for defects: Fundamentals, historical developments, recent applications. Int J Fatigue 2021;151:106407. https://doi.org/10.1016/j.ijfatigue.2021.106407.

[61] Murakami Y. Metal fatigue: Effects of small defects and nonmetallic inclusions. 2019. Doi: 10.1016/C2016-0-05272-5.

[62] BSI Standards Publication. BS 7910: 2019 Guide to methods for assessing the acceptability of flaws in metallic structures 2019.

[63] Foti P, Razavi N, Fatemi A, Berto F. Multiaxial fatigue of additively manufactured metallic components: a review of the failure mechanisms and fatigue life prediction methodologies. Prog Mater Sci 2023;137:101126. https://doi.org/10.1016/j.pmatsci.2023.101126.

[64] Nafar Dastgerdi J, Jaberi O, Remes H. Influence of internal and surface defects on the fatigue performance of additively manufactured stainless steel 316L. Int J Fatigue 2022;163:107025. https://doi.org/10.1016/j.ijfatigue.2022.107025.

[65] Murakami Y, Takahashi K, Yamashita T. Quantitative evaluation of the effect of surface roughness. Transactions of the Japan Society of Mechanical Engineers, Series A 1997;63. https://doi.org/10.1299/kikaia.63.1612.

[66] Macoretta G, Romanelli L, Santus C, Romoli L, Lutey AHA, Uriati F, et al. Modelling of the surface morphology and size effects on fatigue strength of L-PBF Inconel 718 by comparing different testing specimens. Int J Fatigue 2024;181:108120. https://doi.org/10.1016/j.ijfatigue.2023.108120.

[67] Gudić S, Vrsalović L, Kvrgić D, Nagode A. Electrochemical behaviour of ti and ti-6al-4v alloy in phosphate buffered saline solution. Materials 2021;14. https://doi.org/10.3390/ma14247495.

[68] Vladescu A, Pârâu A, Pana I, Cotrut CM, Constantin LR, Braic V, et al. In vitro activity assays of sputtered HAp coatings with SiC addition in various simulated biological fluids. Coatings 2019;9. https://doi.org/10.3390/COATINGS9060389.

[69] Md Saad AP, Jasmawati N, Harun MN, Abdul Kadir MR, Nur H, Hermawan H, et al. Dynamic degradation of porous magnesium under a simulated environment of human cancellous bone. Corros Sci 2016;112:495–506. https://doi.org/10.1016/j.corsci.2016.08.017.

[70] Li Y, Li W, Bobbert FSL, Lietaert K, Dong JH, Leeflang MA, et al. Corrosion fatigue behavior of additively manufactured biodegradable porous zinc. Acta Biomater 2020;106:439–49. https://doi.org/10.1016/j.actbio.2020.02.001.

[71] Vayssette B, Saintier N, Brugger C, El May M. Surface roughness effect of SLM and EBM Ti-6Al-4V on multiaxial high cycle fatigue. Theor Appl Fract Mech 2020;108. https://doi.org/10.1016/j.tafmec.2020.102581.

[72] Sagbas B, Durakbasa NM. Profile and areal surface characterization of additive manufacturing polymer and metal parts. Lecture Notes in Mechanical Engineering 2019. https://doi.org/10.1007/978-3-030-18177-2_22.

[73] Hossain U, Ghouse S, Nai K, Jeffers JRT. Mechanical and morphological properties of additively manufactured SS316L and Ti6Al4V micro-struts as a function of build angle. Addit Manuf 2021;46:102050.

[74] Cao X, Carter LN, Man K, Villapún VM, Giangiorgi L, Cox SC. Improving predictability of additively manufactured Ti-6Al-4 V lattices for orthopaedic devices: a parametric and struts angle study. Mater Des 2024;243. https://doi.org/10.1016/j.matdes.2024.113043.

[75] Dzugan J, Seifi M, Prochazka R, Rund M, Podany P, Konopik P, et al. Effects of thickness and orientation on the small scale fracture behaviour of additively manufactured Ti-6Al-4V. Mater Charact 2018;143:94–109. https://doi.org/10.1016/j.matchar.2018.04.003.

[76] Hogg WW, Jamal M, Zuckschwerdt NW, Hess CM, Bose S, Bandyopadhyay A. Corrosion-fatigue of additively manufactured Ti6Al4V. J Mech Behav Biomed Mater 2026;175:107289. https://doi.org/10.1016/j.jmbbm.2025.107289.

[77] Zheng H, Gai X, Bai Y, Hou W, Li S, Hao Y, et al. Influence of Component size on the Corrosion Behavior of Ti6Al4V Alloy Fabricated by Electron Beam Powder Bed Fusion. Acta Metallurgica Sinica (English Letters) 2024;37:159–68. https://doi.org/10.1007/s40195-023-01609-5.

[78] Murchio S, De Biasi R, Laurenti M, Bonato N, Carmignato S, Benedetti M, et al. Statistical Average Strain Energy Density fatigue estimation of strut-based metamaterials via synthetic as-built CAD digital twins 2026. Doi: 10.21203/rs.3.rs-8740563/v1.

[79] Pascual A, Ortega N, Plaza S, López de Lacalle LN, Ukar E. Analysis of the influence of L-PBF porosity on the mechanical behavior of AlSi10Mg by XRCT-based FEM. J Mater Res Technol 2023;22:958–81. https://doi.org/10.1016/j.jmrt.2022.11.172.

[80] Wits WW, Scolaro E, Amsterdam E, Clare AT. The role of scan strategies in fatigue performance for laser powder bed fusion. CIRP Ann 2022;71:185–8. https://doi.org/10.1016/j.cirp.2022.03.006.